

Genetics and Genomics

Lack of CCDC146, a ubiquitous centriole and microtubule-associated protein, leads to non-syndromic male infertility in human and mouse

Reviewed Preprint

Published from the original preprint after peer review and assessment by eLife.

About eLife's process

Reviewed Preprint posted

12 April 2023

Posted to bioRxiv

1 March 2023

Sent for peer review

27 February 2023

Jana Muroňová, Zine-Eddine Kherraf, Elsa Giordani, Simon Eckert, Caroline Cazin, Amir Amiri-Yekta, Emeline Lambert, Geneviève Chevalier, Guillaume Martinez, Yasmine Neirijnck, Françoise Kühne, Lydia Wehrli, Nikolai Klena, Virginie Hamel, Jessica Escoffier, Paul Guichard, Charles Coutton, Selima Fourati Ben Mustapha, Mahmoud Kharouf, Raoudha Zouari, Nicolas Thierry-Mieg, Serge Nef, Stefan Geimer, Corinne Loeuillet, Pierre Ray, Christophe Arnoult

Institute for Advanced Biosciences, (IAB), INSERM 1209 • Institute for Advanced Biosciences, (IAB) CNRS UMR 5309 • Institute for Advanced Biosciences, (IAB) Université Grenoble Alpes • UM GI-DPI, CHU Grenoble Alpes, F-38000 Grenoble, France • Cell Biology/ Electron Microscopy, University of Bayreuth, 95440 Bayreuth, Germany • UM de Génétique Chromosomique, Hôpital Couple-Enfant, CHU Grenoble Alpes, F-38000 Grenoble, France • Department of Genetic Medicine and Development, University of Geneva Medical School, Geneva 1211, Switzerland • University of Geneva, Department of Molecular and Cellular Biology, Sciences III, Geneva, Switzerland • Human Technopole, 20157 Milan, Italy • Polyclinique les Jasmins, Centre d'Aide Médicale à la Procréation, Centre Urbain Nord, 1003 Tunis, Tunisia • Laboratoire TIMC/MAGe, CNRS UMR 5525, Pavillon Taillefer, Faculté de Médecine, 38700 La Tronche, France

 (https://en.wikipedia.org/wiki/Open_access)

 (<https://creativecommons.org/licenses/by/4.0/>)

Abstract

Genetic mutations are a recurrent cause of male infertility. Multiple morphological abnormalities of the flagellum (MMAF) syndrome is a heterogeneous genetic disease, with which more than 50 genes have been linked. Nevertheless, for 50% of patients with this condition, no genetic cause is identified. From a study of a cohort of 167 MMAF patients, pathogenic bi-allelic mutations were identified in the *CCDC146* gene in two patients. This gene encodes a poorly characterized centrosomal protein which we studied in detail here. First, protein localization was studied in two cell lines. We confirmed the centrosomal localization in somatic cells and showed that the protein also presents multiple microtubule-related localizations during mitotic division, suggesting that it is a microtubule-associated protein (MAP). To better understand the function of the protein at the sperm level, and the molecular pathogenesis of infertility associated with *CCDC146* mutations, two genetically modified mouse models were created: a *Ccdc146* knock-out (KO) and a knock-in (KI) expressing a HA-tagged CCDC146 protein. KO male mice were completely infertile, and sperm exhibited a phenotype identical to our two MMAF patient's phenotype with *CCDC146* mutations. No other pathology was observed, and the animals were viable. CCDC146 expression starts during late spermiogenesis, at the time of flagellum biogenesis. In the spermatozoon, the protein is conserved but is not localized to centrioles, unlike in somatic cells, rather it is present in the axoneme at the level of microtubule doublets. Expansion microscopy associated with the use of the detergent sarkosyl to solubilize microtubule doublets, provided evidence that the protein could be a microtubule inner protein (MIP). At the subcellular level, the absence of CCDC146 affected the formation, localization and morphology of all microtubule-based organelles such as the manchette, the head-tail

coupling apparatus (HTCA), and the axoneme. Through this study, we have characterized a new genetic cause of infertility, identified a new factor in the formation and/or structure of the sperm axoneme, and demonstrated that the CCDC146 protein plays several cellular roles, depending on the cell type and the stages in the cell cycle.

eLife assessment

Muroňová et al. provide **valuable** information about CDCC146 as a centriole and microtubule associated protein essential for sperm flagellar formation and male fertility. Mutations were identified in human patients suffering from MMAF syndrome, but the evidence that these human mutations were causative of the abnormal phenotype is **incomplete**. To further explore the causality, mouse models are generated and the findings from the mouse study, support that the key roles of CCDC146 for microtubule-based structures throughout sperm development in general but requires statical analysis.

Introduction

Infertility is a major health concern, affecting approximately 50 million couples worldwide (1), or 12.5% of women and 10% of men. It is defined by the World Health Organization (WHO) as the “failure to achieve a pregnancy after 12 months or more of regular unprotected sexual intercourse”. In almost all countries, infertile couples have access to assisted reproductive technology (ART) to try to conceive a baby, and there are now 5 million people born as a result of ART. Despite this success, almost half of the couples seeking medical support for infertility fails to successfully conceive and bear a child by the end of their medical care. The main reason for these failures is that one member of the couple produces gametes that are unable to support fertilization and/or embryonic development. Indeed, ART does not specifically treat or even try to elucidate the underlying causes of a couple's infertility, rather it tries to bypass the observed defects. Consequently, when defects in the gametes cannot be circumvented by the techniques currently proposed, ART fails. To really treat infertility, a first step would be to gain a better understanding of the problems with gametogenesis for each patient. This type of approach should increase the likelihood of adopting the best strategy for affected patients, and if necessary, should guide the development of innovative therapies.

Male infertility has several causes, such as infectious diseases, anatomical defects, or a genetic deficiency. Genetic defects play a major role in male infertility, with over 4000 genes thought to be involved in sperm production, of which more than 2000 are testis-enriched and almost exclusively involved in spermatogenesis (2). Mutations in any of these genes can negatively affect spermatogenesis and produce one of many described sperm disorders. The characterization and identification of the molecular bases of male infertility is thus a real challenge. Nevertheless, thanks to the emergence of massively parallel sequencing technologies, such as whole exome sequencing (WES) and whole genome sequencing (WGS), the identification of genetic defects has been greatly facilitated in recent years. As a consequence, remarkable progress has been made in the characterization of numerous human genetic diseases, including male infertility.

Today, more than 120 genes are associated with all types of male infertility (3), including quantitative and qualitative sperm defects. Qualitative spermatogenesis defects impacting sperm morphology, also known as “teratozoospermia” (4; 5), are a heterogeneous group of abnormalities covering a wide range of sperm phenotypes. Among these phenotypes, some

relate to the morphology of the flagellum. These defects are usually not uniform, and patients' sperm show a wide range of flagellar morphologies such as short and/or coiled and/or irregularly sized flagella. Due to this heterogeneity, this phenotype is now referred to as multiple morphological abnormalities of the sperm flagellum (MMAF)(5). Sperm from these patients are generally immotile, and patients are sterile.

Given the number of proteins present in the flagellum and necessary for its formation and functioning, many genes have already been linked to the MMAF phenotype. Study of the MMAF phenotype in humans has allowed the identification of around 50 genes (6) coding for proteins involved in axonemal organization, present in the structures surrounding the axoneme – such as the outer dense fibers and the fibrous sheath – and involved in intra-flagellar transport (IFT). Moreover, some genes have been identified from mouse models, and their human orthologs are very good gene candidates for MMAF, even if no patient has yet been identified with mutations in these genes. Finally, based on the remarkable structural similarity of the axonemal structure of motile cilia and flagella, some MMAF genes were initially identified in the context of primary ciliary dyskinesia (PCD). However, this structural similarity does not necessarily imply a molecular similarity, and only around half (10 of the 22 PCD-related genes identified so far (7)) are effectively associated with male infertility. However, in most cases, the number of patients is very low and the details of the sperm tail phenotype are unknown (7).

We have recruited 167 patients with MMAF. Following whole exome sequencing, biallelic deleterious variants in 22 genes were identified in 83 subjects. The genes identified are *AK7*(8), *ARMC2* (9), *CFAP206* (10), *CCDC34* (11), *CFAP251* (12), *CFAP43* and *CFAP44* (13), *CFAP47* (14), *CFAP61* (15), *CFAP65* (16), *CFAP69* (17), *CFAP70* (18), *CFAP91* (19), *CFAP206* (10), *DNAH1* (20), *DNAH8* (21), *FSIP2* (22), *IFT74* (23), *QRICH2* (24), *SPEF2* (25), *TTC21A* (26) and *TTC29* (27). Despite this success, a molecular diagnosis is obtained in half of the patients (49.7%) with this sperm phenotype, suggesting that novel candidate genes remain to be identified. We have pursued our effort with this cohort to identify further mutations that could explain the patient MMAF phenotype. As such, we have identified bi-allelic truncating mutations in *CCDC146* in two unrelated infertile patients displaying MMAF. *CCDC146* is known to code for a centrosomal protein when heterologously expressed in HeLa cells (28; 29), but minimal information is available on its distribution within the cell, or its function when naturally present. Moreover, this gene has never been associated with any human disease.

The centrosome, located adjacent to the nucleus, is a microtubule-based structure composed of a pair of orthogonally-oriented centrioles surrounded by the pericentriolar material (PCM). The centrosome is the major microtubule-organizing center (MTOC) in animal cells, and as such regulates the microtubule organization within the cell. Therefore, it controls intracellular organization and intracellular transport, and consequently regulates cell shape, cell polarity, and cell migration. The centrosome is also crucial for cell division as it controls the assembly of the mitotic/meiotic spindle, ensuring correct segregation of sister chromatids in each of the daughter cells (30). The importance of this organelle is highlighted by the fact that 3% (579 proteins) of all known human proteins have been experimentally detected in the centrosome (<https://www.proteinatlas.org/humanproteome/subcellular/centrosome>). Centrioles also play essential roles in spermatogenesis and particularly during spermiogenesis. In round spermatids, the centriole pair docks to the cell membrane, whereas the distal centriole serves as the basal body initiating assembly of the axoneme. The proximal centriole then tightly attaches to the sperm nucleus and gradually develops the head-to-tail coupling apparatus (HTCA), linking the sperm head to the flagellum (31). In human and bovine sperm, the proximal centriole is retained and the distal centriole is remodeled to produce an 'atypical' centriole (32); in contrast, in rodents, both centrioles are degenerated during epididymal maturation (33). Despite the number of proteins making up the centrosome, and its importance in sperm differentiation and flagellum formation, very

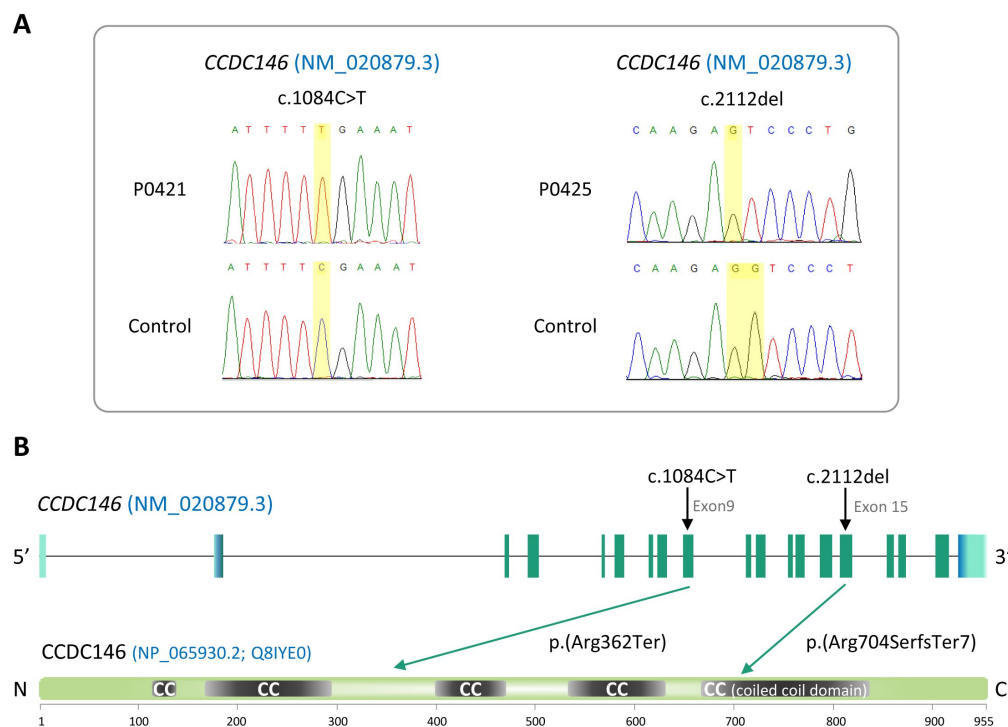
few centrosomal proteins have been linked to MMAF in humans – so far only CEP135 (34), CEP148 (35) or DZIP1 (36). Moreover, some major axonemal proteins with an accessory location in the centrosome, such as CFAP58 (37) and ODF2 (38; 39), have also been reported to be involved in MMAF syndrome. Other centrosomal proteins lead to MMAF in mice, these include CEP131 (40) and CCDC42 (41). The discovery that MMAF in humans is linked to CCDC146, known so far as a centrosomal protein, adds to our knowledge of proteins important for axoneme biogenesis.

In this manuscript, we first evaluated the localization of endogenous CCDC146 during the cell cycle in two types of cell cultures, immortalized cells and primary human foreskin fibroblasts. To validate the gene candidate and improve our knowledge of the corresponding protein, we also generated two mouse models. The first one was a *Ccdc146* KO model, with which to study the impact of lack of the protein on the general phenotype, and in particular on male reproductive function using several optical and electronic microscopy techniques. The second model was a HA-tagged CCDC146 model, with which we studied the localization of the protein in different cell types. Data from these genetically modified mouse models were confirmed in human sperm cells.

Results

1/ WES identifies *CCDC146* as a gene involved in MMAF

We performed whole exome sequencing (WES) to investigate a highly-selected cohort of 167 MMAF patients previously described in (9). The WES data was analyzed using an open-source bioinformatics pipeline developed in-house, as previously described (42). From these data, we identified two patients with homozygous truncating variants in the *CCDC146* (coiled-coil domain containing 146) gene, NM_020879.3 (Figure 1A). No other candidate variants reported to be associated with male infertility was detected in these patients. This gene is highly transcribed in both human and mouse testes (Supp Figure 1). The first identified mutation is located in exon 9/19 and corresponds to c.1084C>T, the second is located in exon 15/19 and corresponds to c.2112Del (Figure 1B). The c.1084C>T variant is a nonsense mutation, whereas the single-nucleotide deletion c.2112Del is predicted to induce a translational frameshift. Both mutations were predicted to produce premature stop codons: p.(Arg362Ter) and p.(Arg704serfsTer7), respectively, leading either to the complete absence of the protein, or to the production of a truncated and non-functional protein. The two mutations are therefore most-likely deleterious (Figure 1B). Both variants were absent in our control cohort and their minor allele frequencies (MAF), according to the gnomAD v3 database, were 6.984×10^{-5} and 0 respectively. The presence of these variants and their homozygous state were verified by Sanger sequencing, as illustrated in Figure 1. Taken together, these elements strongly suggest that mutations in the *CCDC146* gene could be responsible for the infertility of these two patients and the MMAF phenotype.



Variants are annotated according to HGVS recommendations.

Figure 1:

Identification of two CCDC146 gene variants in MMAF patients

(A) Position of the observed variants in both probands. Electropherograms indicating the homozygous state of the identified variant: variant c.1084C>T is a non-sense mutation, and c. c.2112Del is a single- nucleotide deletion predicted to induce a translational frameshift. (B) Structure of the canonical CCDC146 gene transcript showing the position of the variants and their impact on translation.

2/Ccdc146 knock-out mouse model confirms that lack of CCDC146 is associated with MMAF

To validate the hypothesis that CCDC146 deficiency leads to MMAF and male infertility, we produced by CRISPR/Cas9 two mouse lines carrying each a frameshift mutation in *Ccdc146* (ENSMUST00000115245). (Supp Figure 2). We analyzed the reproductive phenotype of the edited animals from the F2 generation and found that homozygous males were infertile and reproduced the MMAF phenotype like the two patients carrying the homozygous variants in the orthologous gene. Based on these findings, we restricted our study to a strain with a 4-bp deletion in exon 2 (c.164_167delTTCG).

The KO mice were viable without apparent defects. The reproductive phenotypes of male and female mice were explored. WT or heterozygous animals and KO females were fertile, whereas KO males were completely infertile (Figure 2A). This infertility is associated with a 90% decrease in epididymal sperm concentration (from ~30- to ~3-million) (Figure 2B) and an almost complete absence of motility (Figure 2C). Closer examination revealed sperm morphology to be strongly altered, with a typical MMAF phenotype and marked defects in head morphology (Figure 2E) indicative of significantly impaired spermiogenesis. In addition, testicle weight relative to whole body weight was significantly lower (Figure 2D), suggesting a germ cell rarefaction in the seminiferous epithelia due to high apoptosis level. A study of spermatogenic cell viability by TUNEL assay confirmed this hypothesis, with a significant increase in the number of positive cells in *Ccdc146* KO animals (Supp Figure 3). Comparative histological studies (Figure 3) showed that on sections of spermatogenic tubules, structural and shape defects were present from the elongating spermatid stage in KO mice, with almost complete disappearance of the flagella in the lumen. At the epididymal

level, transverse sections of the epididymal tubules from KO males contained almost no spermatozoa, and the tubules were filled with an acellular substance.

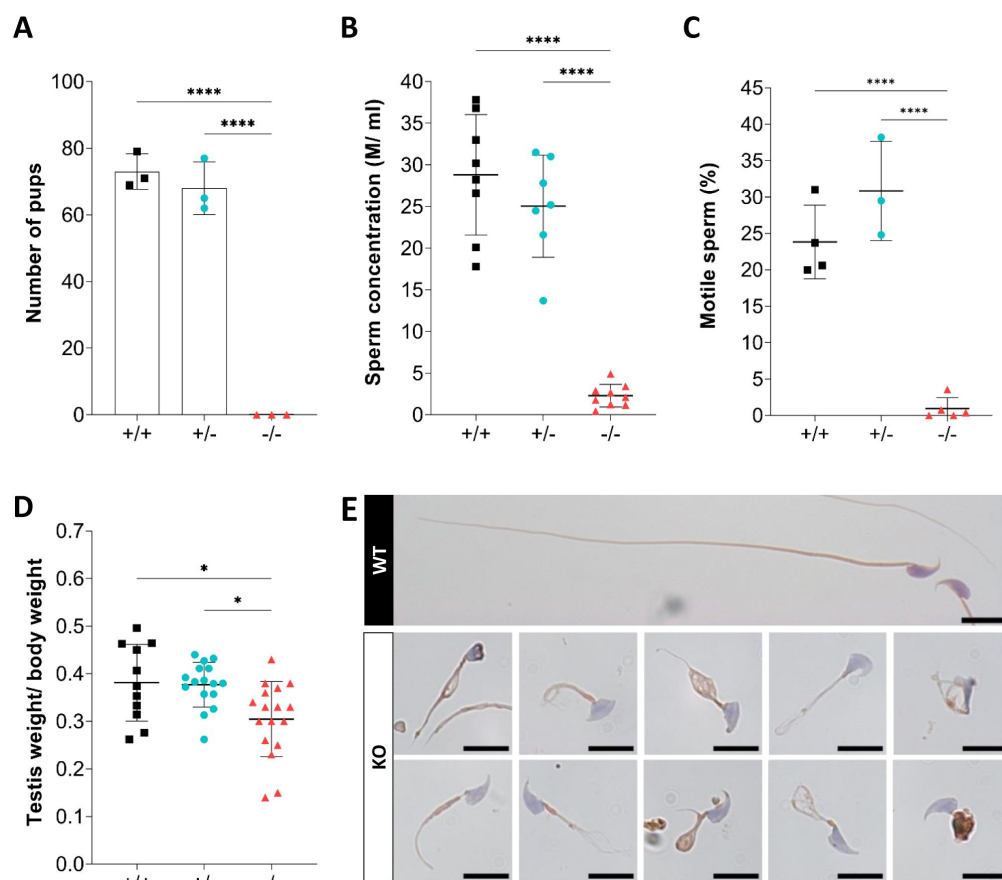


Figure 2:

Ccdc146* KO mice are infertile and KO sperm exhibit a typical “multiple morphological abnormalities of the flagellum (MMAF)” phenotype.** (A) Number of pups produced by wild-type (+/+, WT), *CCDC146* heterozygote (+/-) and *CCDC146* knock-out (-/-, KO) males (3 males per genotype) after mating with fertile WT females (2 females per male) over a period of three months. (B) Sperm concentration and (C) sperm mobility. (D) Comparison of testis weights (mg). (E) Illustration of WT and KO sperm morphologies stained with Papanicolaou and observed under optic microscopy. Statistical comparisons were based on ordinary one-way ANOVA tests (*

$p < 0.0001$; **** $p < 0.001$, ** $p < 0.01$, * $p < 0.05$). Scale bar of images represents 10 μ m.

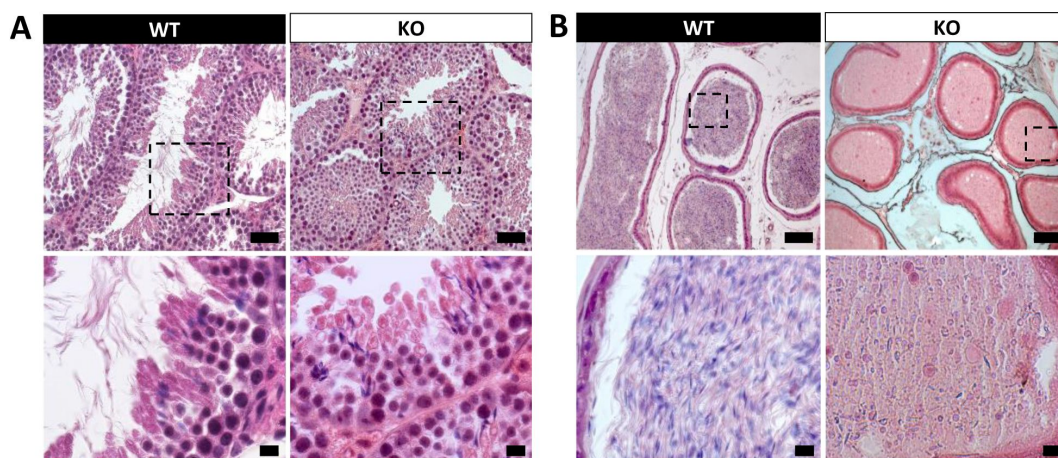


Figure 3:

Histological evidence that spermiogenesis is disrupted in *Ccdc146* KO males and leads to a strong decrease in sperm concentration in the epididymis.

(A) Transversal sections of WT and KO testis stained with hematoxylin and eosin. The upper images show the sections at low magnification (Scale bars: 50 µm) and the lower images are an enlargement of the dotted square (scale bars: 10 µm). In the KO, spermatid nuclei were very elongated and no flagella were visible within the seminiferous tubule lumen. (B) Transversal sections of WT and KO epididymis stained with hematoxylin and eosin. Despite similar epididymis section diameters in WT and KO testes, KO lumen were filled with round cells and contained few spermatozoa with abnormally- shaped heads and flagella. The upper images show the sections at low magnification (scale bars 50 µm) and the lower images are an enlargement of the dotted square (scale bars 10 µm).

3/ CCDC146 codes for a centriolar protein

CCDC146 has been described as a centriolar protein in immortalized HeLa cells (28; 29). To confirm this localization, we performed immunofluorescence experiments (Figure 4). First, we focused on the centrosome. In HEK-293T cells, using an antibody recognizing centrin (anti-centrin Ab) as a centriole marker and an anti-CCDC146 Ab, CCDC146 was shown to colocalize with centrioles. However, the signal was not strictly localized to centrioles, as peri-centriolar labeling was clearly visible. As this labeling pattern suggests the presence of centriolar satellite proteins, we next performed co-labeling with an antibody recognizing PCM1, a canonical centriolar satellite marker (43). Once again, the colocalization was only partial (Supp Figure 4). Based on these observations, CCDC146 has a unique localization profile that may indicate specific functions.

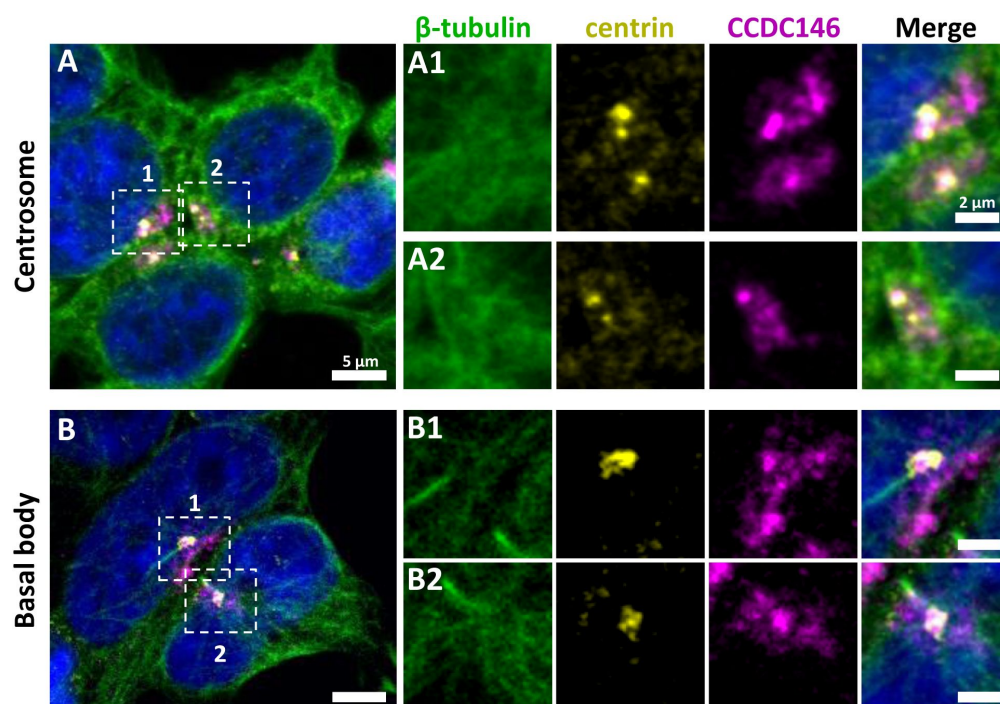


Figure 4:

CCDC146 has a centriolar and pericentriolar localization in interphase somatic HEK-293T cells.

HEK-293T cells were immunolabeled for β -tubulin (green), centrin (yellow) and CCDC146 (magenta). DNA was stained with Hoechst (blue). (A) CCDC146 localized to centrioles and/ or to the pericentriolar material in interphase cells. The centrosomes of two cells are shown enlarged in A1 and A2. (B) In serum starved

cells with primary cilia, CCDC146 localizes to the basal body of primary cilia. The basal body of two cells are shown enlarged in B1 and B2. CCDC146 is also present as dotted signal resembling the pattern for centriolar satellite proteins. Scale bars on zoomed images: 2 μ m.

4/ CCDC146 co-localizes with multiple tubulin-based organelles

Interestingly, our immunofluorescence experiments revealed that CCDC146 labeling was not strictly limited to centrosomes – other tubulin-containing cellular substructures were also labeled, particularly structures emerging during cell division (Figure 5). Thus, the mitotic spindle was labeled at its base and at its ends. The co-labeling intensified in the midzone during chromatid separation. Finally, the separation structure between the two cells, the midbody, was also strongly stained. As HEK-293T cells are an immortalized cell line, we therefore verified that this labeling pattern was not due to an aberrant expression profile and that it also reflected the situation in primary cell lines. Identical labeling profiles were observed in freshly-prepared Human foreskin fibroblasts (HFF cells) (Supp Figure 5).

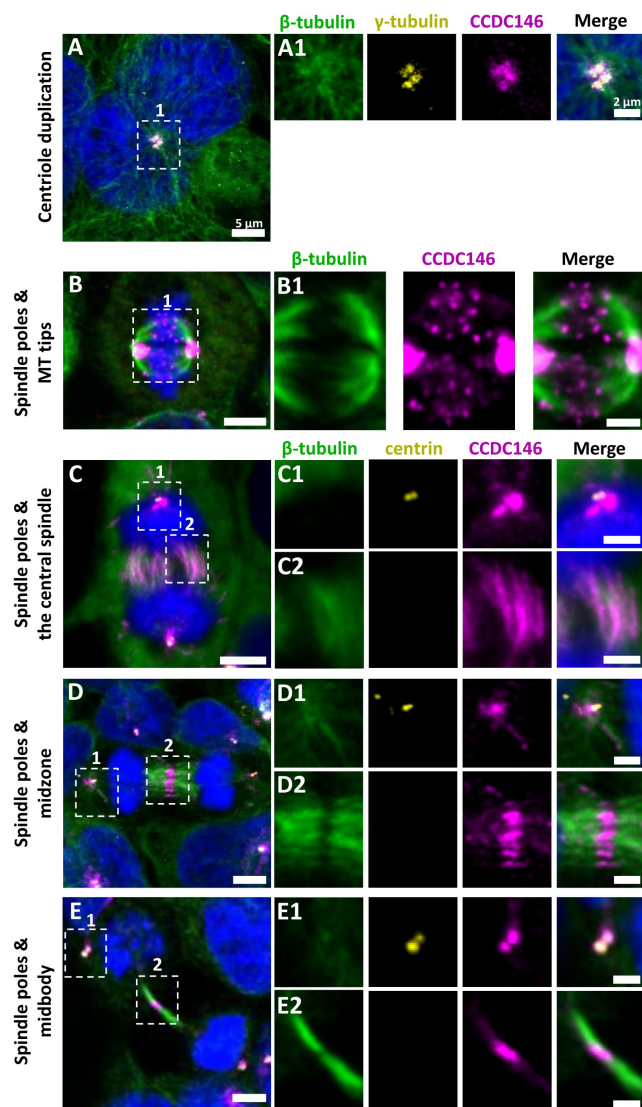


Figure 5:

CCDC146 is a microtubule-associated protein (MAP) associating with microtubule-based structures throughout the cell cycle.

HEK-293T cells were immunolabeled with anti- β -tubulin (green), anti-centrin (yellow), and anti-CCDC146 (magenta) Abs. DNA was stained with Hoechst (blue). In synchronized HEK-293T cells, CCDC146 is observed associated with (A) mother centrioles and their corresponding procentrioles during centriole duplication. (B) In non-synchronized cells, CCDC146 is observed associated with microtubule tips during metaphase, (C) the central spindle during (C) anaphase and (D) telophase, and (E) the midbody during cytokinesis. Images on the right show the enlargement of the dotted square in the left image. Scale bar of zoomed images 2 μ m.

5/ Expression profile of CCDC146 during the first wave of spermatogenesis in mouse

From our immunofluorescence analysis of somatic cell lines, it was clear that CCDC146 expression is associated with the cell cycle. In the testis, a wide variety of cell types co-exist, including both somatic and germline cells. The germline cells can be further subcategorized into a wide variety of cells, some engaged in proliferation (spermatogonia), others in meiosis (spermatocytes), or in differentiation (spermatids). To better understand the role of CCDC146 in spermatogenesis, and thus how its absence leads to sperm death and malformation, we initially studied its expression during the first wave of spermatogenesis (44) and sought to detect the protein in testis extracts at several postnatal timepoints and in the mature epididymal spermatozoon. Results from this study should shed light on when CCDC146 is required for sperm formation. Surprisingly, RT-PCR failed to detect *Ccdc146* transcripts in proliferating spermatogonia on day 9 after birth (Figure 6A). Transcription of *Ccdc146* started on day 18, concomitantly with the initiation of meiosis 2. Expression peaked on day 26, during the differentiation of spermatids. We also wished to explore the expression of the protein. To overcome a lack of specific antibodies recognizing mouse CCDC146, a transgenic mouse was created: (hemagglutinin) sequence was inserted by the CRISPR/Cas9 system into the coding sequence of the *Ccdc146* gene between the two first codons to produce a tagged

protein at the N-terminus domain (Supp Figure 6). This insertion induced no phenotypic changes, and both female and male mice were viable with normal fertility. Tag insertion was validated by Western blotting (WB) (Figure 6B). The theoretical MW of the tagged protein is around 116.2 kDa ($115.1 + 1.1$); the observed MW was slightly higher, suggesting some post-translational modifications. Using these mice, testicular extracts from several postnatal timepoints and from epididymal spermatozoa were analyzed (Figure 6B). In accordance with RT-PCR experiments, bands corresponding to HA-tagged CCDC146 were detectable at D26 and 35, and in epididymal sperm (Figure 6C). The protein is therefore present during spermatid differentiation and conserved in mature sperm. The absence of the protein during spermatogonia proliferation suggests a new function for CCDC146 in sperm cells.

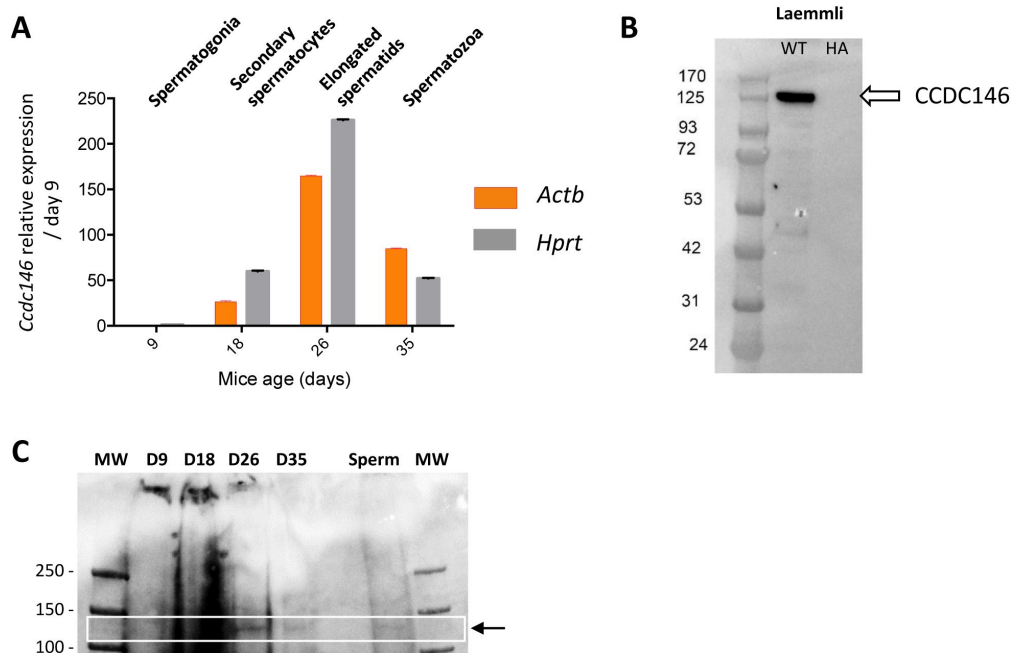


Figure 6:

CCDC146 is expressed in late spermatocyte and in spermatids; CCDC146 protein is present in spermatids and in epididymal spermatozoa in mouse.

(A) mRNA expression levels of *Ccdc146* relative to *Actb* and *Hprt* in CCDC146-HA mouse pups' testes. Extremely low expression was detected at day 9, corresponding to testes con-

taining spermatogonia and Sertoli cells only. *Ccdc146* expression was observed from postnatal day 18 (formation of secondary spermatocytes), peaked at day 26 (formation of elongated spermatids), and subsequently decreased from day 35 (formation of spermatozoa), suggesting that *Ccdc146* is particularly expressed in elongated spermatids during spermatogenesis. (B) Western blot of HA-tagged and WT sperm showing the specific band (arrow) corresponding to HA-tagged CCDC146 (CCDC146-HA) in epididymal whole sperm. (C) Western blot of HA-tagged testis extracts at different postnatal days. The presence of HA-tagged CCDC146 was revealed by an anti-HA Ab. Faint bands at the expected molecular weight are observed at D26, D35 and in epididymal sperm.

6/ In sperm, CCDC146 is present in the flagellum, not in the centriole

To attempt to elucidate the function of CCDC146 in sperm cells, we next studied its localization by IF in human and murine spermatozoa. We focused successively on the anterior segment (head, neck and beginning of the intermediate piece) of the sperm and then on the flagellum. In humans, the spermatozoon retains its two centrioles (32), and they are observable in the neck, as shown by anti-centrin and anti-tubulin labeling (Figure 7A1-3). No colocalization of the CCDC146 label with centrin was observed on human sperm centrioles, suggesting that the protein is not present in or around this structure. However,

two unexpected labeling events were observed: sub-acrosomal labeling and labeling of the midpiece. At the flagellum level, faint staining was observed along the whole length (Figure 7A4).

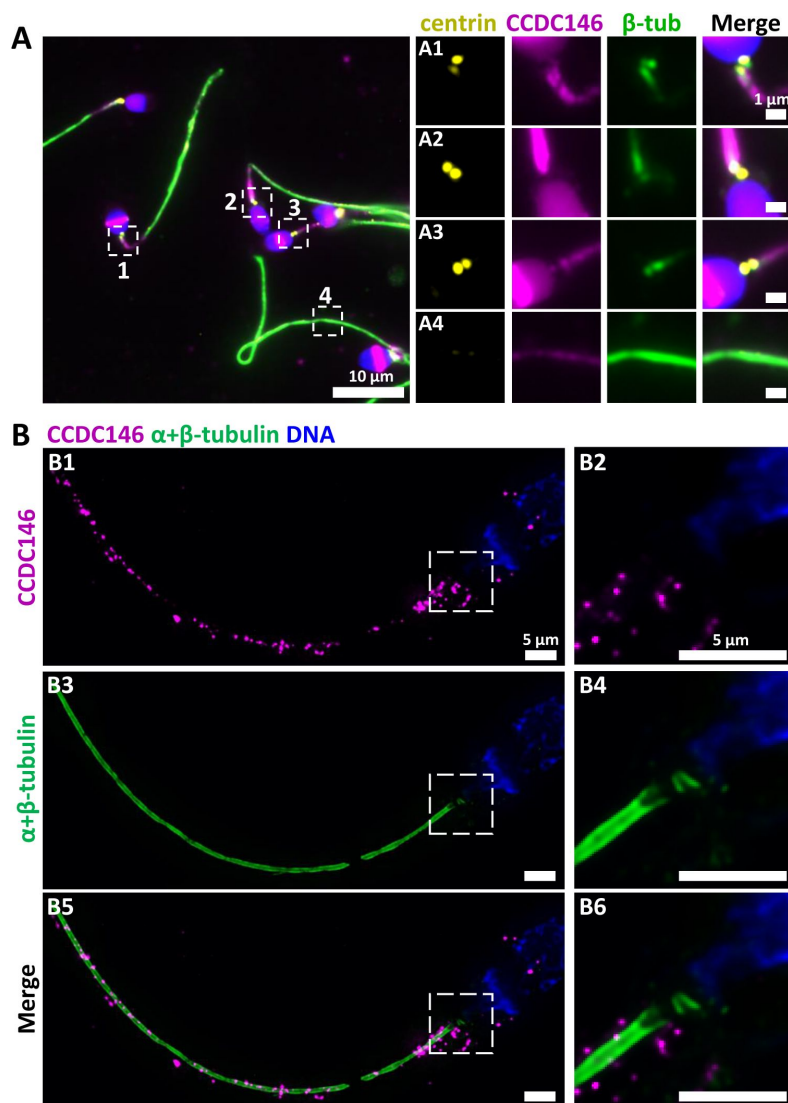


Figure 7:

CCDC146 localizes to the flagellum but not to the centrioles of ejaculated human spermatozoa.

(A) Human ejaculated sperm were immunolabeled with Abs recognizing centrin (yellow), CCDC146 (magenta), and β -tubulin (green). DNA was stained with Hoechst (blue). (A1-A3) enlargement of dotted square focused on sperm neck: no colocalization between CCDC146 and centrin. (A4) A faint signal for CCDC146 is present along the length of the sperm flagellum. Scale bar of zoomed images: 1 μ m. (B) Human ejaculated sperm observed by expansion microscopy. Sperm were immunolabeled with anti-CCDC146 (magenta) and anti- β -tubulin (green), and DNA was stained with Hoechst (blue). B1 and B5 show strong staining for CCDC146 in the axoneme, B3 showing the localization of the axoneme through tubulin staining. B2, B4 and B6 show enlargements of the dotted square focused on the sperm neck. CCDC146 did not colocalize with the centrioles at the base of the axoneme. The CCDC146 staining observed probably corresponds to non-specific labeling of mitochondria.

To enhance resolution, ultrastructure expansion microscopy (U-ExM), an efficient method to study in detail the ultrastructure of organelles (45), was used (Figure 7B). The localization of the two centrioles was perfectly visible following anti-tubulin labeling, and was confirmed by co-labeling with an anti-POC5 Ab (Supp Figure 7). Once again, no CCDC146 labeling was observed on sperm centrioles (Figure 7B3), confirming the conventional IF results. Moreover, U-ExM unveiled that the observed CCDC146 midpiece staining (Figure 7A) seems in fact associated with isolated structures, which we hypothesize could be mitochondria, now visible by expansion (Figure 7B1). This suggests that the labeling on the midpiece observed in IF corresponds to non-specific mitochondrial labeling. This conclusion is supported by the fact that the same isolated structures were also labeled with anti-POC5 Ab (Supp Figure 7). In contrast, at the flagellum level, clear punctiform labeling was observed along the whole length of the main piece (Figure 7B1-B3), confirming that the protein is present in the sperm flagellum.

The same experiments were performed on murine epididymal spermatozoa. For this study, we used the mouse model expressing HA-tagged CCDC146 protein. It should be noted that

unlike in humans, in mice, centrioles are no longer present in epididymal spermatozoa (33). In conventional IF, using an anti-HA Ab, labeling was observed along the whole flagellum (Figure 8A). The strong HA-labeling in the midpiece was clearly non-specific, as the signal was still present when secondary antibodies were used alone (Supp Figure 8). In expansion microscopy, unexpectedly, the mouse flagellum presented breaks that most likely resulted from the expansion procedure (Figure 8B). Interestingly, strong HA-labeling was observed at the level of these breaks suggesting that CCDC146 epitopes are buried inside the axonemal structure and become accessible mostly on blunt or broken microtubule doublets. The same pattern was observed with three different anti-HA antibodies (Figure 8A-C). To confirm the presence of CCDC146 in the flagellum, sperm flagella were purified after mild sonication, and protein extracts were analyzed by WB (Figure 8D). In the flagella fraction, the HA Ab revealed a single band at around 120 kDa, thus confirming the flagellar localization of CCDC146 in both human and mouse sperm.

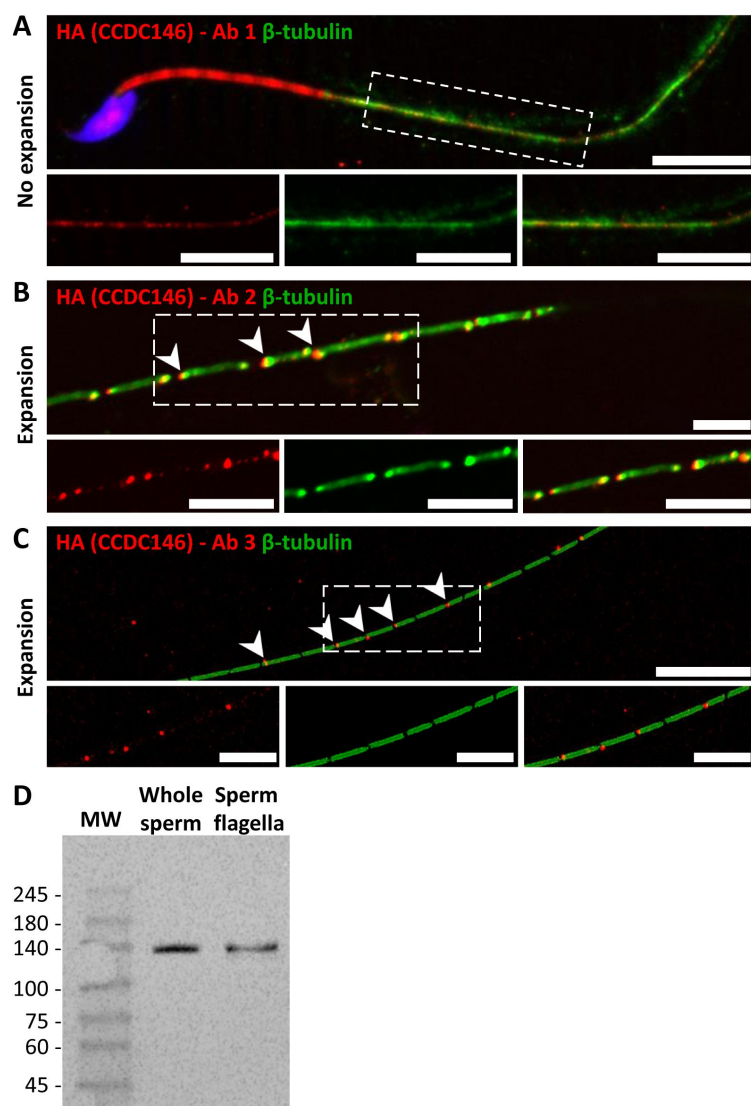


Figure 8:

CCDC146 localizes to the flagellum of mouse epididymal spermatozoa.

(A) Mouse epididymal spermatozoa observed with conventional IF. CCDC146-HA sperm were labeled with anti-HA #1 (red) and anti- β -tubulin (green) Abs. DNA was stained with Hoechst (blue). The upper image shows the sperm with merged immunostaining, and the lower images, the staining (red, green, and merge) observed in the principal piece of the flagellum (Scale bars 10 μ m). (B) Mouse epididymal spermatozoa observed with expansion microscopy. CCDC146-HA sperm were immunolabeled with anti-HA #2 (red) and anti- β -tubulin (green) Abs. DNA was stained with Hoechst (blue). The upper image shows the sperm with merged immunostaining. The lower images show the staining (red, green, and merge) observed in the principal piece of the flagellum. Strong punctiform signals were observed at the level of axonemal breakages induced by the expansion process. White arrows indicate the zones of the micro breaks (Scale bars correspond to 10 μ m). (C) Similar experiment performed with a third anti-HA Ab (#3). Scale bars 10 μ m. (D) Western blot of whole sperm and flagella fraction extracts. The presence of CCDC146-HA was revealed by an anti-HA Ab.

7/ CCDC146 labeling associates with microtubule doublets

We next wanted to determine whether CCDC146 staining was associated with the axoneme or accessory structures of the flagellum (outer dense fibers or fibrous sheath), and if yes, whether it was associated with microtubule doublets or the central pair. To do so, we used U-

ExM on human sperm and quantified the relative position of each CCDC146 dot observed (outside the axoneme, outer left and right; microtubule doublets left and right and central pair – [Figure 9A-C](#)). The distribution of localizations was summarized in two bar graphs, generated for two distinct sperm cells. Labeling was preferentially located on the right and left doublets ([Figure 9D](#) and [9F](#)), indicating that CCDC146 associates more with microtubule doublets. Analysis of protein distribution in mice was not easy, because signal tended to concentrate at breaks. Nevertheless, on some spermatozoa with frayed microtubule doublets, i.e. with the flagellum taking on the shape of a hair, we could find that isolated doublets carried the punctiform labeling confirming the results of analyses on human spermatozoa ([Figure 9G](#)). Taken together, these results from mouse and human sperm demonstrate that CCDC146 is an axonemal protein, probably associated with microtubule doublets.

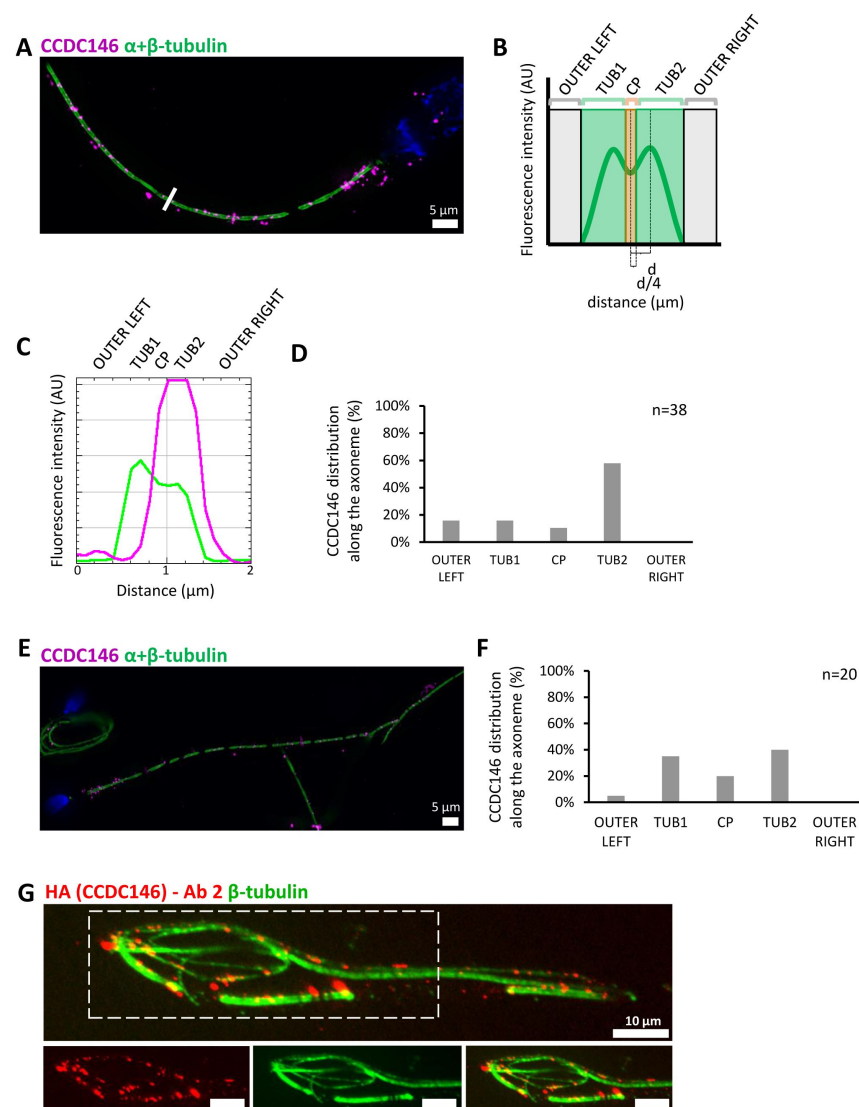


Figure 9:

CCDC146 localizes to the microtubule doublets of the axoneme in human and mouse

(A) Sperm was double-stained with anti-tubulin Ab (green) and anti-CCDC146-Ab (magenta) and observed by expansion microscopy. (B) The position of the CCDC146 signal with respect to the tubulin signal was measured along the entire flagellum. CCDC146 signals were localized to different compartments of the axoneme by the following method: the green signal is quite characteristic with two peaks corresponding to the left and right microtubule doublet, it identifies five axonemal compartments (left outer, left doublet, central pair, right doublet, and right outer). For each CCDC146 signal (magenta dots), the flagellum was perpendicularly cut (example, white bar in A) and the tubulin and CCDC146 signals measured to assign each CCDC146 signal to a localization area. (C) Example of a measurement obtained at the right bar shown in (A). (D) Histogram showing the distribution of CCDC146 labeling in ejaculated human sperm 1, presented in (A). (E) Ejaculated human sperm double-stained with anti-tubulin Ab (green) and

anti-CCDC146-Ab (magenta). (F) Histogram showing how CCDC146 labeling distributed in ejaculated human sperm 2. (G) Flagellum of a mouse epididymal spermatozoa observed with expansion microscopy. CCDC146-HA sperm were immunolabeled with anti-HA #2 (red) and anti-β-tubulin (green). The upper image shows the sperm with merged immunostaining, and the lower images, the staining (red, green, and merge) observed in the principal piece of the flagellum. Scale bars 10 μm.

8/ CCDC146 could be a Microtubule Inner Protein (MIP)

The presence of extensive labeling at axoneme breaks suggests that the antigenic site is difficult to access in an intact flagellum. We therefore hypothesized that CCDC146 could be a MIP. MIPs are generally resistant to solubilization by detergents. However, N-lauroylsarcosine (sarkosyl) can solubilize microtubule doublets, with increasing concentrations destabilizing first the A-tubule, then the B-tubule (46; 47). Microtubule solubilization allows release of the MIPs contained within the tubules, and the method is recognized (48; 49). To test whether our hypothesis that CCDC146 is a MIP, we treated spermatozoa from HA-tagged CCDC146 mice with sarkosyl and performed a WB on the

supernatant (Figure 10A). The protein was effectively solubilized, leading to the appearance of bands at around 120 kDa on an SDS-PAGE gel following migration of extracts from sperm treated with 0.2 and 0.4% sarkosyl concentrations. Interestingly, a second band around 90 kDa was also immunodecorated by anti-HA antibody in the sarkosyl treated sample, a band not present in the protein extracts from WT males. The other detergents and buffers tested – RIPA, CHAPS or Tris-HCl – barely solubilized CCDC146 or led to no solubilization (Figure 10B). This result confirms the unique action of sarkosyl on CCDC146 and strengthens the hypothesis that the protein is localized in the lumen of tubules. To confirm the action of sarkosyl on the accessibility of the antigenic site, murine spermatozoa were labeled with an anti-HA antibody after treatment with sarkosyl or no treatment. CCDC146 labeling was significantly increased in the presence of sarkosyl (Figure 10C). The full image panel including secondary Ab control experiments can be found in Supp Figure 9.

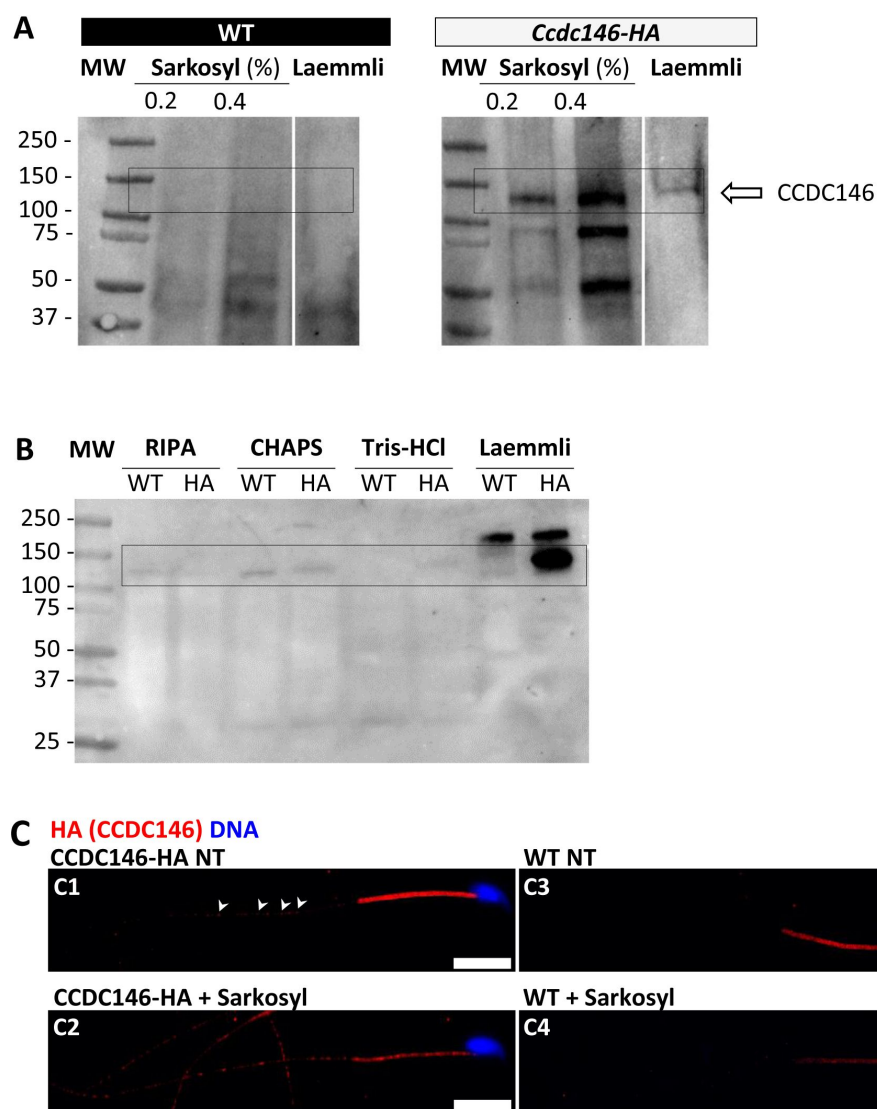


Figure 10:

CCDC146 could be a microtubule inner protein in sperm: evidence from sarkosyl treatment

(A) Western blot of WT and CCDC146-HA sperm extract solubilized with N-lauroylsarcosine (sarkosyl), an anionic detergent. Sarkosyl was used at increasing concentrations (0.2, and 0.4%). The presence of CCDC146-HA was detected by an anti-HA Ab. (B) Western blot of WT and CCDC146-HA sperm extracts solubilized with alternative detergents (RIPA, CHAPS, Tris-HCl) and whole sperm extract solubilized in Laemmli. The presence of CCDC146-HA was revealed by an anti-HA Ab. (C) Epididymal CCDC146-HA sperm (C1-C2) and WT sperm (C3-C4), treated with sarkosyl (5 min, 0.2% sarkosyl) or not (NT), were immunostained to reveal the HA-tag (red) and counterstained with Hoechst (blue). (C1) Without treat-

ment, a faint CCDC146 signal (white arrow heads) is observed along the flagellum from CCDC146-HA sperm. (C2) Treatment with sarkosyl enhanced the CCDC146-HA signal along the sperm flagellum. (C3) HA signal in WT non-treated (NT) sperm is present in the midpiece only, suggesting that this signal is not specific. (C4) The HA signal in WT sperm is not enhanced by sarkosyl treatment. Scale bars 10 μ m.

9/ KO models show defects in tubulin-made organelles

To better characterize the function of CCDC146 in mouse sperm, we went on to perform a detailed morphological analysis of tubulin-made organelles by IF, and examined the morphological defects induced by the absence of CCDC146 at the subcellular level by scanning and/or transmission electron microscopy. This work was performed on immature testicular sperm and on seminiferous tubule sections from adult WT and KO males. Mouse testicular sperm were used because they still contain centrioles that become disassembled as sperm transit through the epididymis (50). We mainly focused our analyses on the centrioles, the manchette, and the axoneme.

The connecting piece between the head and the flagellum, known as the sperm head-tail coupling apparatus (HTCA), is a complex structure containing several substructures including both centrioles, the capitulum and the segmented columns. The distal centriole is embedded in the segmented column and the axoneme emerges from the distal centriole. This structure has a specific shape when observed by scanning electron microscopy (Figure 11A). In *Ccdc146* KO sperm, the connecting piece was severely damaged (Figure 11A). In WT testicular sperm, IF experiments show that the centrioles, identified by anti-tubulin Ab, are very close to each other and adjacent to the capitulum (Figure 11B). In *Ccdc146* KO males, centriole separation was visible in numerous spermatozoa (Figure 11B3, B4), with the structures located far away from the connecting piece (Figure 11B5) or duplicated (Figure 11B6). Interestingly, the overall structure of the HTCA under construction in spermatids, observed by TEM, was conserved in *Ccdc146* KO spermatids, with the presence of both centrioles, containing nine triplets of microtubules, the proximal centriole and its adjunct, as well as accessory cytoskeletal structures, including the capitulum and the segmented columns (Figure 12AB). Remarkably, in a very large proportion of sections, no singlet or doublet of microtubules emerged from the distal KO centriole, suggesting that the process of tubulin polymerization is somehow hampered in these cells (Figure 12A). The absence of microtubules at the end of the distal centriole was confirmed by analysis of serial sections of the sperm centrioles (Figure 12C). Moreover, the defects observed in IF experiments, such as duplication, or defective attachment to the nuclear membrane, were frequently confirmed in TEM images (Supp Figure 10). Such defects were not observed in WT spermatids.

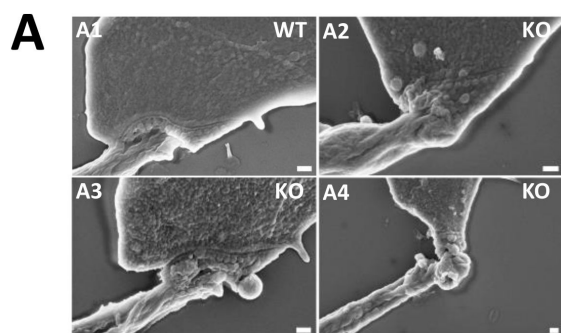
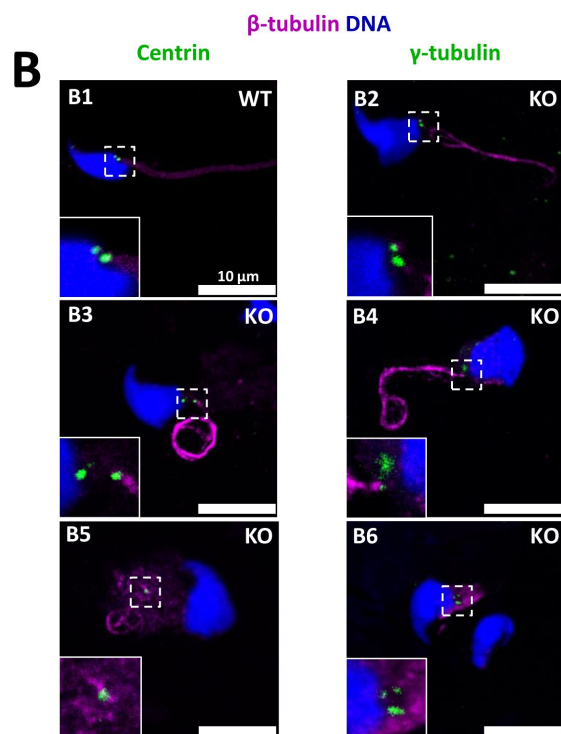


Figure 11:

The absence of CCDC146 causes defects of the head-tail coupling apparatus in epididymal spermatozoa and duplication and mislocalization of centriole in testicular sperm.

(A) Scanning electron microscopy of WT and *Ccdc146* KO epididymal spermatozoa showed aberrant head morphologies and irregular head-tail coupling apparatus (HTCA) linking the sperm head with the flagellum. (B) Testicular spermatozoa from WT (B1) and *Ccdc146* KO (B2-B6) mice immunolabeled with anti- β -tubulin (magenta) and anti-centrin (B1-B3) or anti- γ -tubulin (B4-B6) (green) Abs. Centrioles appeared to be normal (B2) in some spermatozoa, separated but partially attached to the head (B3, B4), completely detached from the sperm head (B5) or duplicated (B6).



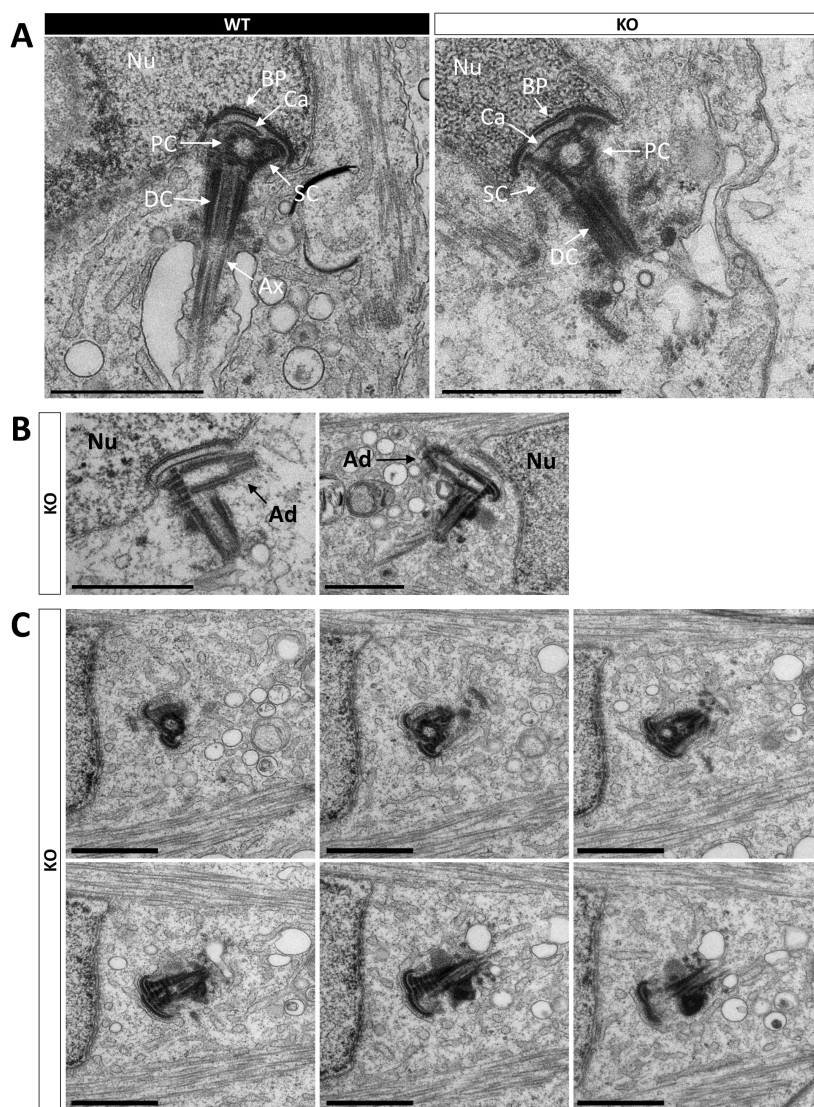


Figure 12:

Absence of elongation of axonemal microtubules at the base of the distal centriole.

(A) In WT spermatids, the proximal centriole (PC) is linked to the base of the compacting nucleus (Nu) through the basal plate (BP) and the capitulum (Ca), and the distal centriole (DC) is embedded in the segmented column (SC). All these sperm-specific cytoskeletal structures make up the HTCA. At the base of the distal centriole, axonemal microtubules (MT) grow. In *Ccdc146* KO elongating spermatids, the overall structure of the HTCA is conserved, with the presence of the centrioles and the accessory cytoskeletal structures. However, no axonemal microtubules are visible. (B) The adjunct (Ad) of the proximal centriole is also preserved in *Ccdc146* KO spermatids. (C) Serial sections of the HTCA of a *Ccdc146* KO spermatid confirm the absence of axonemal microtubules at the base of the distal centriole during spermatid elongation. Scale bars 1 μ m.

Manchette formation – which occurs from the round spermatid to fully-elongated spermatid stages – was next studied by IF using β -tubulin Ab. Simultaneously, we monitored formation of the acrosome using an antibody binding to DPY19L2 (Figure 13). Initial acrosome binding at step III was not disrupted, and we observed no differences in the caudal descent of the acrosome during subsequent steps (III- VIII). The development of the manchette in between stages IX-XII was not hampered, but noticeable defects appeared indicating defective manchette organization– such as a random orientation of the spermatids and abnormal acrosome shapes. Finally, at step I, the manchette was clearly longer and wider than in WT cells, suggesting that the control of the manchette biogenesis is defective. In TEM, microtubules in the manchette were clearly visible surrounding the compacting nucleus of elongating spermatids. However, many defects such as marked asymmetry and enlargement were visible (Figure 14). The manchette normally anchors on the perinuclear ring, which is itself localized just below the marginal edge of the acrosome and separated by the groove belt (51). In KO spermatids, the perinuclear ring was no longer localized in the vicinity of the acrosome and was often spread into the cytoplasm, providing a large nucleation structure for the manchette (Figure 14 D-F, red arrows), which explains its width and irregularity.

A

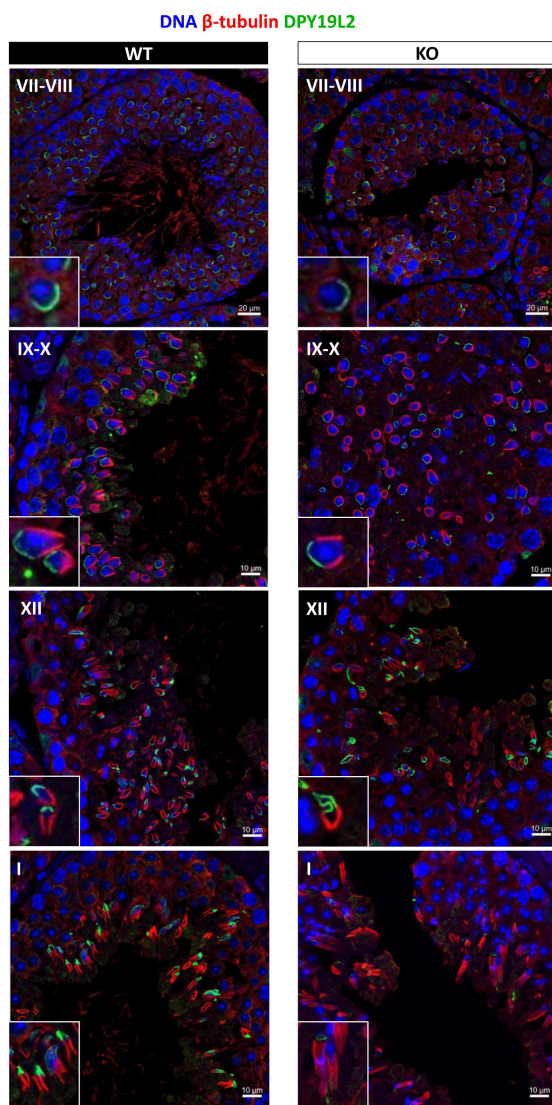


Figure 13:

Analysis of stages of spermatogenesis by IF reveals acrosome formation and manchette elongation defects.

Cross sections of WT and *Ccdc146* KO testes showing different stages of mouse spermatogenesis (I, VII-XII). Stages were determined by double immunostaining for β -tubulin (red) and DPY19L2 (green; acrosome localization), and DNA was stained with Hoechst (blue). (A) Very few mature spermatozoa lined the lumen at stage VII-VIII in the KO. Cell orientations appear random from stage IX-X in the KO and the tubules contain more advanced spermatid stages. The acrosome of elongating KO spermatids had become abnormal by stage XII, and the manchette of elongated spermatids at stage I was longer in the KO compared with the WT. (B) Typical spermatids from stages I-XII, showing details of acrosome formation and manchette elongation. Scale bars stages VII-VIII 20 μ m, scale bars IX-X, XII and I 10 μ m.

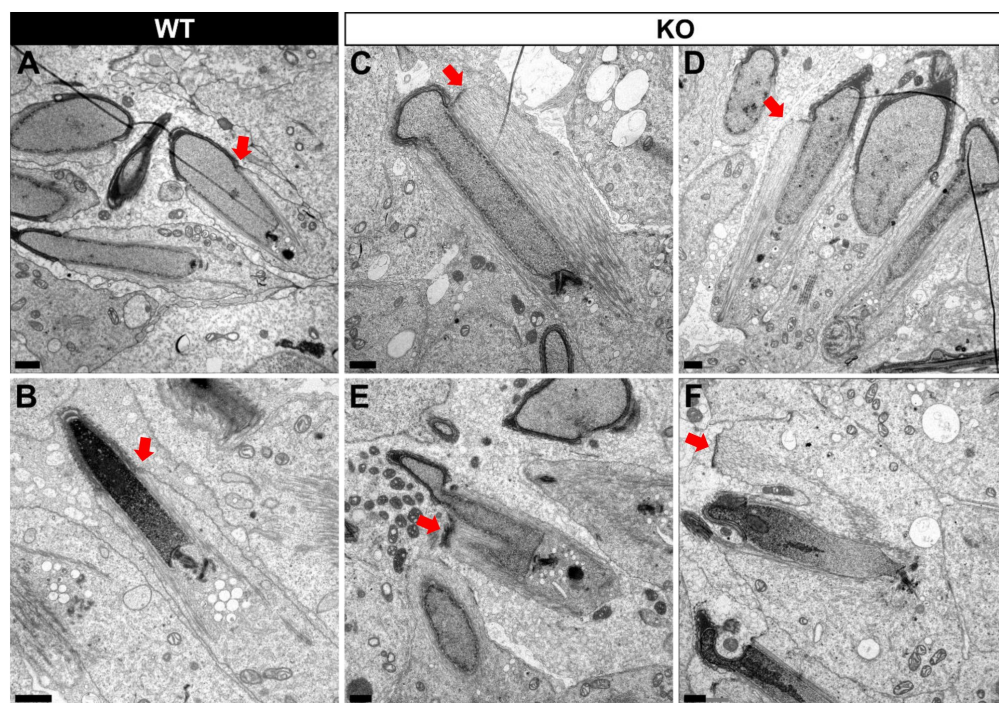


Figure 14:

TEM of elongating spermatids from *Ccdc146* KO male shows ultrastructural defects of the manchette.

(A, B) Ultrastructural analysis of the manchette in WT elongating spermatids shows the normal thin perinuclear ring, anchored below the acrosome and allowing a narrow array of microtubules to anchor. (C-F) In elongating spermatids from *CCDC146* KO animals, the perinuclear ring was ab-

normally broad, usually located on one side of the spermatid (red arrows), creating an asymmetric and wide bundle of microtubules. The resulting manchette was wider and often longer than in WT animals. (E, F) The tubulin nucleation location was sometimes ectopic in the KO and coincided with irregularly shaped sperm heads.

Numerous defects were also observed in the axoneme. These axoneme defects were generally similar to the defects observed in other MMAF mouse models, with disorganization of the axoneme structure (Figure 15A) accompanied by fragmentation of the dense fibers and their random arrangement in cell masses anchored to the sperm head (Figure 15C). The absence of emerging singlet or doublet microtubules at the base of the distal centriole leads to a complete disorganization of the flagellum and the presence of notably dense fiber rings devoid of internal tubulin elements (Figure 15BC).

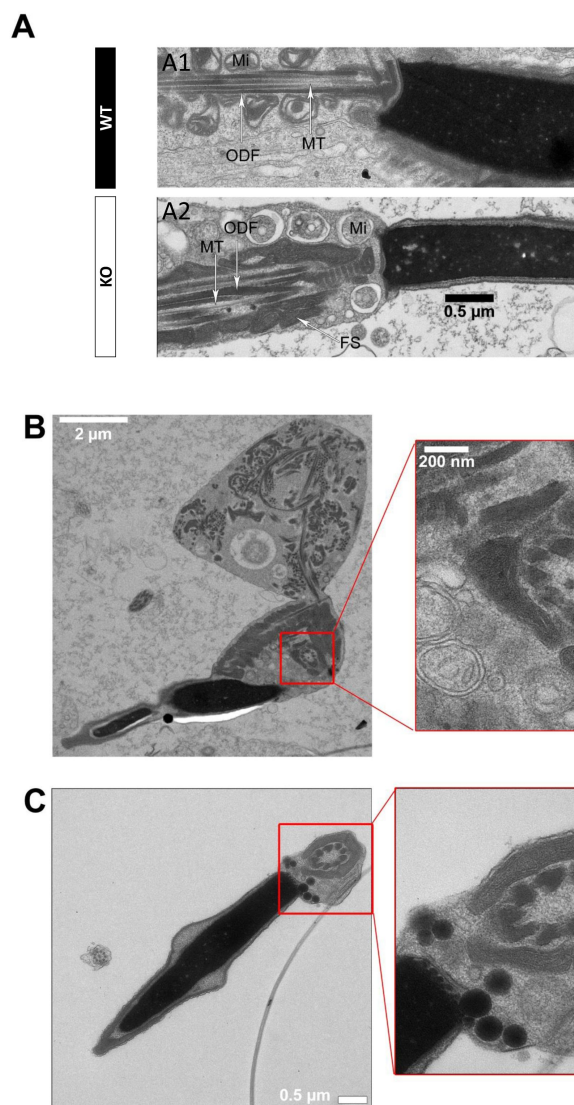


Figure 15:

The axonemes of *Ccdc146* KO spermatids present multiple defects visible under TEM.

(A1) A longitudinal section of a WT flagellum shows a typical structure of the principal piece, with outer dense fibers (ODF) at the periphery, microtubules (MT) in the center, and mitochondria (Mi) aligned along the flagellum. (B1) A longitudinal section of a *Ccdc146* KO flagellum shows a disorganized midpiece, with altered mitochondria, the presence of an amorphous fibrous sheath (FS) and altered microtubules. (B) Longitudinal section of a *Ccdc146* KO sperm showing dispersed and non-assembled flagellar material in a cytoplasmic mass. The right-hand image is the enlargement of the red square, showing the presence of an external ring of mitochondria surrounding an outer dense fiber ring devoid of microtubular material. (C) Longitudinal section of another *Ccdc146* KO sperm showing a similar abnormal midpiece structure. The right-hand image is the enlargement of the red square, showing the presence of an external ring of mitochondria surrounding an outer dense fiber ring devoid of microtubular material.

Finally, the shape of the nucleus presented numerous abnormalities (Supp Figure 11). The emergence of head defects was concomitant to the implantation of the manchette, with no defects observed on round spermatids at stages III-VIII. Unexpectedly, a distortion was created in the center of the nucleus at the anterior pole, causing the formation of a bilobed compacted nucleus (Supp Figure 13E-G) containing visible vacuoles.

Discussion

This study allowed us to identify and validate the involvement of a new candidate gene in male infertility, *CCDC146*. This gene was first described in mice by our team earlier this year, in the context of a research project on the different types of genetic causes of sperm abnormalities in mouse (52). However, no data other than the sperm phenotype (MMAF) was presented in this initial report. In this paper, we present for the first time, the evidence of the presence of mutations in humans and a description of the localization of the protein in somatic and germ cells. We also examined the lesion spectrum at the subcellular level, to obtain a detailed view of the molecular pathogenesis associated with defects in this gene.

1/ Genetic complexity of MMAF

It is essential to characterize all genes involved in male infertility. Therefore, the characterization of a new gene involved in MMAF syndrome is not just "one more gene". First, it further confirms that MMAF syndrome is a heterogeneous recessive genetic disease, currently associated with defects in more than 50 genes. Second, it helps direct the diagnostic strategy to be directed during genome-wide searches. The type of profiling required for MMAF is very different from that performed for instance for cystic fibrosis, where one mutation is responsible for more than 50% of cases. Third, the discovery of all genes involved in MMAF is important in the context of oligogenic heterozygous inheritance of sperm abnormalities in human (52). Indeed, a homozygous deleterious mutation is found in only half of all MMAF patients, suggesting that other modes of inheritance must be involved. Only by establishing an extended list of genes linked to MMAF will it be possible to determine whether oligogenic heterozygous inheritance is a relevant cause of this syndrome in humans. Finally, some of the genes involved in MMAF syndrome are also involved in ciliary diseases (7). By further exploring MMAF-type infertility, we can hope to enhance our understanding of another underlying pathology. Although the vast majority of patients with PCD are diagnosed before 5 years of age (53), one study showed that in a cohort of 240 adults with a mean age of 36 years (36 ± 13) presenting with chronic productive cough and recurrent chest infections, PCD was identified for the first time in 10% of patients (54). This result suggests that infertility diagnosis can occur before PCD diagnosis, and consequently that infertility management might improve PCD diagnosis and care.

2/ Functional complexity of CCDC146

The results presented in this report show striking differences in localization of CCDC146 between somatic and germ cells. Our results show that the protein displays several subcellular localizations, which vary according to the cell cycle, and the cell nature. In somatic cells, the protein is mostly associated with the centrosome and other microtubular structures – in particular the mitotic spindle – at the end of microtubules and at the level of the kinetochore and the midbody. These observations identify CCDC146 as a microtubule-associated protein (MAP). In contrast, in spermatozoa, IF images indicate that CCDC146 is an axonemal protein that could be localized in the microtubule doublets. Moreover, the CCDC146 signal was enhanced when sperm were treated with the sarkosyl detergent, used to identify microtubule inner proteins (MIP). Finally, expansion microscopy revealed a strong signal in mouse sperm at the point of axoneme rupture. Taken together, these elements suggest that CCDC146 may be a MIP. Despite its broad cellular distribution, the association of CCDC146 with tubulin-dependent structures is remarkable. However, centrosomal and axonemal localizations in somatic and germ cells, respectively, have also been reported for CFAP58 (37; 55), thus the re-use of centrosomal proteins in the sperm flagellar axoneme is not unheard of. In addition, 80% of all proteins identified as centrosomal are found in multiple localizations (<https://www.proteinatlas.org/humanproteome/subcellular/centrosome>). The ability of a protein to home to several locations depending on its cellular environment has been widely described, in particular for MAP. The different localizations are linked to the presence of distinct binding sites on the protein. For example, MAP6 binds and stabilizes microtubules, through Mc modules, and associates with membranes and neuroreceptors through palmitoylated cysteines. MAP6 can also localize in the microtubule lumen, in its role as MIP, thanks to its Mn modules. Finally, in addition to its associations with subcellular compartments and receptors, the presence of proline-rich domains (PRD) in the MAP6 sequence, allows it to bind to SH3-domain-containing proteins, and thus triggering activation of signaling pathways (56). Another example of a protein with multiple localizations is CFAP21, which is a MIP but also a cytosolic calcium sensor. In the latter capacity, CFAP21 modulates the interaction of STIM1 and ORAI1 upon depletion of calcium

stores (57; 58). These examples illustrate the complexity of function of some multiple-domain proteins.

The fact that CCDC146 can localize to multiple subcellular compartments suggests that it also contains several domains. Interestingly, a PF05557 motif (Pfam mitotic checkpoint protein, <https://www.ebi.ac.uk/interpro/protein/UniProt/E9Q9F7/>) has been identified in the mouse CCDC146 sequence between amino acids 130 and 162. Proteins belonging to the “mitotic spindle checkpoint” monitor correct attachment of the bipolar spindle to the kinetochores. The presence of this motif likely explains the ability of CCDC146 to localize to cell cycle-dependent subcellular compartments containing tubulin. However, the most important structural motifs identified in CCDC146 are the coiled-coil domains. Although coiled-coils play a structural role in a variety of protein interactions, their presence in CCDC146 remains mysterious, and how they contribute to its function remains to be elucidated. Nevertheless, this motif is compatible with a MIP function for this protein, since several MIP proteins including CCDC11 (FAP53), CCDC19 (FAP45), and CCDC173 (FAP210) are coiled-coil proteins (57). It is worth noting that the ortholog of *CCDC146* in *Chlamydomonas*, *MBO2*, codes for a protein required for the beak-like projections of doublets 5 and 6, located inside the lumen of the tubule B (59), in the proximal part of the *Chlamydomonas* flagellum. Although no beak-like projections are present in the mammalian axoneme, the location inside the tubule seems to be evolutionarily conserved. A more recent study of *MBO2* showed that the protein is also present all along the flagellum of *Chlamydomonas* and is tightly associated with microtubule doublets (60). These observations support our results showing association of CCDC146 with this axonemal structure.

The results presented here also show a striking difference in the phenotype induced by the lack of the protein in somatic and male germ cells. This protein is essential for spermatogenesis, and its absence leads to immotile non-functional sperm and to complete infertility in both humans and mice. Conversely, both patients and *Ccdc146* KO mice seem to be healthy and present no other conditions such as primary ciliary dyskinesia (PCD). CCDC146, despite its wide expression profile in many tissues therefore seems to be dispensable except during spermatogenesis. Nevertheless, because this protein is localized on the tips of the spindle and may be involved in mitotic checkpoints, its absence may lead to late proliferative disorders. This hypothesis is supported by the fact that *CCDC146* is reported to be down-regulated in thyroid cancer (61). The link between infertility and risk of cancer was recently underlined, with mutations found in genes like *FANCM* (62). Therefore, it would be interesting to monitor aging in *Ccdc146* KO mice and to study their life expectancy and cancer rates compared to WT mice.

3/ Absence of CCDC146 in sperm centriole

Several proteomics studies of the sperm centriole identified CCDC146 as a centrosome-associated protein in bovine sperm (28; 63), a species where centrioles are present in ejaculated sperm. Using a different methodological approach, based on IF with conventional and expansion microscopy, we observed no CCDC146 signal in centrioles from testicular mouse and ejaculated human sperm. The same result was obtained with two different types of antibodies: with human sperm, we used a commercial anti-CCDC146 Ab, whereas with mouse sperm we used several anti-HA antibodies. The same IF approach allowed us to clearly identify the sperm centrosome using a number of antibodies such as anti-POC5 and anti-beta tubulin, ruling out a possible failure of our IF protocol. It is worth noting that centrosomal proteins were isolated from whole flagella using several strategies including sequential use of multiple detergents, and that the centrosomal proteins were purified in the last fractions. These results indicate that CCDC146 is in fact barely soluble in conventional buffers, which could explain why it is co-purified with the centrosomal fraction in proteomics studies.

4/ TEM reveals that lack of CCDC146 severely impacts microtubule-based organelles

No morphological defects were observed before the elongating spermatid stage, and in round spermatids, the acrosome started to spread on the nucleus in a normal way (Figure 13). Morphological defects appeared clearly from the onset of spermatid elongation. This result indicates that the protein is only necessary for late spermiogenesis, from the phase corresponding to flagellum biogenesis. All the organelles composed mainly of tubulin were strongly affected by the absence of the protein.

The manchette structure in elongating *Ccdc146* KO spermatids was asymmetric, abnormally broad, and ectopic, leading to the formation of aberrantly-shaped sperm heads. So far, manchette defects have been associated with defects in intra-flagellar transport (IFT), and intra-manchette transport (IMT) (64). CCDC146 was only localized to the sperm axoneme by IF, and no signal was observed in the manchette, suggesting that CCDC146 is probably not involved in the transport machinery. Moreover, our results indicated that the manchette was remarkably long in elongated spermatids. A similar phenotype was observed in Katanin80-deficient animals (65). Katanin80 is a microtubule-severing enzyme that is important for manchette reduction. Interestingly, the absence of WDR62, a scaffold protein involved in centriole duplication, leads to defective katanin80 expression, and the presence of elongated manchettes in mice (66). In combination with our results, this detail suggests that the manchette's structure and its reduction are influenced by centrosomal proteins, possibly through katanin defects. The precise molecular link between CCDC146 and manchette assembly and reduction remains to be identified.

The HTCA was also aberrant in *Ccdc146* KO spermatids. Centrioles in elongating spermatids were frequently displaced from their implantation fossa at the nuclear envelope. We observed some correctly lodged centrioles in round spermatids; however, we are unable to determine with certainty whether the majority of centrioles failed to correctly attach or whether they detached from the nuclear envelope during spermatid elongation. Defects in cohesion of the HTCA have been associated with the acephalic spermatozoa syndrome, and were shown to involve a number of proteins such as SUN5, SPATA6 and ODF1 [(4), (67)–(69)]. Here, we did not observe any sperm decapitation, suggesting that CCDC146 is involved in a different pathway controlling the HTCA. Moreover, elongating *Ccdc146* KO spermatids displayed supernumerary centrioles. Abnormal centriole numbers have also been reported in the absence of a few other centrosome-associated proteins including DZIP1 (36) and CCDC42 (41), and of microtubule-regulating proteins such as katanin like-2 (70) and tubulin deglutamylase CCP5 (71).

Studies of the spermiogenesis defects observed in different models deficient for centrosomal proteins show some common features such as abnormal manchette and duplicated centrosomes. The absence of these proteins does not appear to be directly responsible for these defects, rather it seems to modify the expression of microtubule regulatory proteins such as katanins (65; 66; 70). These modifications could explain the pleiotropic effect of the absence of CCDC146 on microtubule-based organelles.

In conclusion, by characterizing the genetic causes of human infertility, we not only improve the diagnosis and prognosis of these pathologies but also pave the way for the discovery of new players in spermatogenesis. We are constantly adding to the number of proteins present in the flagella of the mammalian spermatozoa that are necessary for its construction and functioning. This study showed that CCDC146, a protein previously described as a centrosomal protein in somatic and germ cells, localizes in spermatozoa's axonemal microtubule doublets. The presence of CCDC146 in somatic cells' centrosomes gives weight to

the idea of a centrosome with a dynamic composition, allowing it to fulfill its multitude of functions throughout all the phases of cellular life.

Material and methods

Human subjects and controls

We analyzed WES data from a cohort of 167 MMAF individuals previously established by our team (9). All individuals presented with a typical MMAF phenotype characterized by severe asthenozoospermia (total sperm motility below 10%) with at least three of the following flagellar abnormalities present in >5% of the spermatozoa: short, absent, coiled, bent or irregular flagella. All individuals had a normal somatic karyotype (46,XY) with normal bilateral testicular size, normal hormone levels and secondary sexual characteristics. Sperm analyses were carried out in the source laboratories during routine biological examination of the individuals according to World Health Organization (WHO) guidelines (72). Informed and written consents were obtained from all the individuals participating in the study and institutional approval was given by the local medical ethical committee (CHU Grenoble Alpes institutional review board). Samples were stored in the Fertithèque collection declared to the French Ministry of health (DC-2015-2580) and the French Data Protection Authority (DR-2016-392).

Sanger sequencing

CCDC146 single nucleotide variants identified by exome sequencing were validated by Sanger sequencing as previously described (9). PCR primers used for each individual are listed in Table supplementary 1.

Cell culture

HEK-293T (Human Embryonic Kidney) and HFF (Human Foreskin Fibroblasts) cells were grown in D10 consisting in DMEM with GlutaMAX (Dulbecco's Modified Eagle's Medium, Sigma Aldrich) supplemented with 10% heat-inactivated fetal bovine serum (FBS, Life Technologies) and 10% of penicillin-streptomycin (Sigma Aldrich) in a 5% CO₂ humidified atmosphere at 37 °C. HEK-293T cells were divided twice weekly by 1/10 dilution. HFFs cells were divided 1/5 one time a week.

Ethics statement

Breeding and experimental procedures were carried out in accordance with national and international laws relating to laboratory animal welfare and experimentation (EEC Council Directive 2010/63/EU, September 2010). Experiments were performed under the supervision of C.L. (agreement 38 10 38) in the Plateforme de Haute Technologie Animale (PHTA) animal care facility (agreement C3851610006 delivered by the Direction Départementale de la Protection des Populations) and were approved by the ethics committee of the PHTA and by the French government (APAFIS#7128- 2016100609382341.v2).

Generation of *Ccdc146* KO and HA-tagged *CCDC146* mice

Ccdc146 KO mice were generated using the CRISPR/Cas9 technology as previously described (52). Briefly, to maximize the chances of generating deleterious mutations, two gRNAs located in two distinct coding exons located at the beginning of the targeted gene were used.

For each gene, the two gRNAs (5'-CCT ACA GTT AAC ATT CGG G-3' and 5'-GGG AGT ACA ATA TTC AGT AC-3'), respectively targeting exons 2 and 4, were inserted into two distinct plasmids, each plasmid also contained the Cas9 sequence (Supp Figure 2). The Cas9 gene was controlled by a CMV promoter and the gRNA and its RNA scaffold by a U6 promoter. Full plasmids (pSpCas9 BB-2A-GFP (PX458)) containing the specific sgRNA were ordered from Genescript (<https://www.genscript.com/crispr-synthetic-sgrna.html>). Both plasmids were co-injected into the zygotes' pronuclei at a concentration of 2.5 ng/mL. Plasmids were directly injected as delivered by the supplier, without in vitro production and purification of Cas9 proteins and sgRNA.

Ccdc146-HA knock-in mice were also generated by CRISPR/Cas9. Twenty-seven nucleotides encoding the HA (hemagglutinin) tag (5'-TAC CCA TAC GAT GTT CCA GAT TAC GCT TAG-3') were inserted immediately after the start codon of Ccdc146. One plasmid containing one sgRNA (5'-TAC TTT AGA ACT GTG AAA AA-3') and Cas9 was injected (5 ng/μL) with a single-stranded DNA (150 nucleotides, 50 ng/μL) as a template for the homology directed repair (HDR) Appendix figure 6. PCR primers used for genotyping are listed in Table supplementary 1. Transgenic CCDC146 strains were bred in the Grenoble university animal platform (HTAG) and housed under specific-pathogen-free conditions. Animals were euthanized by cervical dislocation at the indicated ages.

Phenotypic analysis of *Ccdc146* KO mice

Fertility test – Three adult males of each genotype were housed individually with two fertile WT B6D2 females for 12 weeks. The date of birth and the number of pups were recorded.

Sperm analysis – Epididymal sperm were obtained by making small incisions in the mouse caudae epididymides placed in 1 mL of warm M2 medium (Sigma Aldrich), and the sperm were allowed to swim up for 10 min at 37 °C. Sperm samples (10 μL) were used for Computer-assisted semen analysis (CASA, Hamilton Thorn Research, Beverley, MA, USA) using a 100-μm-deep analysis chamber (Leja Products B.V., Nieuw-Vennep, the Netherlands). A minimum of 100 motile sperm was recorded in each assay. The remaining sperm samples were washed in 1X phosphate buffered saline (PBS, Life technologies), 10 μL were spread onto slides pre-coated with 0.1% poly-L-lysine (Eprelia), fixed in 70% ethanol (Sigma Aldrich) for 1 h at room temperature (RT) and submitted to a papanicolaou staining (WHO laboratory manual) to assess sperm morphology. Images were obtained using a Zeiss AxioImager M2 fitted with a 40X objective (color camera AxioCam MRC) and analyzed using ZEN (Carl Zeiss, version 3.4).

Testis and epididymides histology

Testis and epididymides samples from 8-16-week-old mice were fixed for 24 h in PBS/4% PFA (Electron Microscopy Sciences), dehydrated in a graded ethanol series, embedded in paraffin wax, sectioned at 5 μm and placed onto Superfrost slides (Fischer scientific). For both, slides were deparaffinated and rehydrated prior to use. Tissue morphology and structure were observed after coloration by Mayer's hematoxylin and eosin phloxine B (WHO protocols) using a Zeiss AxioImager M2 (color camera AxioCam MRC).

Terminal deoxynucleotidyl transferase dUTP nick-end labeling (TUNEL) assay on testes

Testes samples from three adult individuals for each genotype were analyzed. Apoptotic cells in testis sections were identified using the Click-iT™ Plus TUNEL Assay kit (Invitrogen) in line with the manufacturer's instructions. DNA strand breaks for the positive control were

induced by DNase I treatment. Each slide contained up to eight testis sections. DNA was stained with Hoechst (2 µg/mL). Images were acquired and reconstituted using a Zeiss Axioscan Z1 slide scanner and analyzed by Fiji (73). The total number of seminiferous tubules and the number of tubules containing at least one TUNEL-positive cell were counted in each testis section.

Conventional Immunofluorescence (IF)

Somatic Cells – HEK-293T or HFFs (10 000 cells) were grown on 10-mm coverslips previously coated with poly-D-lysine (0.1 mg/mL, 1 h, 37 °C, Gibco) placed in a well on a 24-well plate. After 24 h, cells were directly fixed with ice-cold methanol (Sigma Aldrich) for 10 min. After washing twice in PBS, non-specific sites were blocked with PBS/5% FBS/5% NGS (normal goat serum, Life technologies) for 1 h at RT. After washing three times in PBS/1% FBS, primary antibody was added in PBS/1% FBS and incubated overnight at 4 °C. Coverslips were washed three times in PBS/1% FBS before adding secondary antibody in PBS/1% FBS and incubating for 2 h at RT. After washing three times in PBS, nuclei were stained with 2 µg/mL Hoechst 33342 in PBS (Sigma Aldrich). Coverslips were once again washed three times in PBS, then carefully placed on Superfrost slides (cells facing the slide) and sealed with nail polish.

Spermatogenic cells – Seminiferous tubules were isolated from mouse testes (8–16 weeks old). After removing of the tunica albuginea, the testes were incubated at 37 °C for 1 h in 3 mL of a solution containing (mM): NaCl (150), KCl (5), CaCl₂ (2), MgCl₂ (1), NaH₂PO₄ (1), NaHCO₃ (12), D-glucose (11), Na-lactate (6), HEPES (10) pH 7.4, and collagenase type IA (1 mg/mL – Sigma Aldrich). Tubules were rinsed twice in collagenase-free medium and cut into 2-mm sections. Spermatogenic cells were obtained by manual trituration and filtered through a 100-µm filter. The isolated cells were centrifuged (10 min, 500 g), resuspended in 500 µL PBS and 50 µL was spread onto slides pre-coated with 0.1% poly-L-lysine (EpreDia) and allowed to dry. Dried samples were fixed for 5 min in PBS/4% PFA. After washing twice in PBS, slides were placed in PBS/0.1% Triton/5% BSA (Euromedex) for 90 min at RT. Following two washes in PBS, the primary antibody was added in PBS/1% BSA overnight at 4 °C. After washing three times in PBS/1% BSA, secondary antibody was added in PBS/1% BSA for 2 h at RT. After washing three times in PBS, nuclei were stained with 2 µg/mL Hoechst 33342 in PBS (Sigma Aldrich) and slides were mounted with DAKO mounting media (Agilent).

Testis sections – After deparaffination and rehydration, testis sections were subjected to heat antigen retrieval for 20 min at 95 °C in a citrate-based solution at pH 6.0 (VectorLabs). Tissues were then permeabilized in PBS/0.1% Triton X-100 for 20 min at RT. After washing three times in PBS (5 min each), slides were incubated with blocking solution (PBS/10% BSA) for 30 min at RT. Following three washes in PBS, slides were incubated with primary antibodies in PBS/0.1% Tween/5% BSA overnight at 4 °C. Slides were washed three times in PBS before applying secondary antibodies in blocking solution and incubating for 2 h at RT. After washing in PBS, nuclei were stained with 2 µg/mL Hoechst 33342 in PBS (Sigma Aldrich) for 5 min at RT. Slides were washed once again in PBS before mounting with DAKO mounting media (Agilent).

Spermatozoa (conventional protocol) - Mouse spermatozoa were recovered from the caudae epididymides. After their incision, sperm were allowed to swim in 1 mL of PBS for 10 min at 37 °C. They were washed twice with 1 mL of PBS 1X at 500 g for 5 min, and 10 µL of each sample was smeared onto slides pre-coated with 0.1% poly-L-lysine (EpreDia). Sperm were fixed in PBS/4% PFA for 45 s, washed twice in PBS and permeabilized in PBS/0.1% Triton for 15 min at RT. After incubation in PBS/0.1% Triton/2% NGS for 2 h at RT, primary antibody was added in PBS/0.1% Triton/2% NGS overnight at 4 °C. After washing three times in PBS/0.1% Triton, the secondary antibody was applied in PBS/0.1% Triton/2% NGS for 90 min at RT. Slides were washed three times in PBS before staining nuclei with 2 µg/mL Hoechst

33342 in PBS (Sigma Aldrich). Slides were washed once in PBS before mounting with DAKO mounting media (Agilent).

For human spermatozoa, the protocol was based on that of Fishman *et al.* (32). Straws were thawed at RT for 10 min and resuspended in PBS. Sperm were washed twice in 1 mL of PBS (10 min, 400 g), 50 μ L was spread onto slides pre-coated with 0.1% poly-L-lysine and left to dry. Dry slides were fixed in 100% ice-cold methanol for 2 min and washed twice in PBS. Cells were permeabilized in PBS/3% Triton X-100 (PBS-Tx) for 1 h at RT. Slides were then placed in PBS-Tx/1% BSA (PBS-Tx-B) for 30 min at RT. Immunofluorescence was performed as for mouse spermatozoa. Sperm were then incubated with primary antibodies in PBS-Tx-B overnight at 4 °C. After washing three times in PBS-Tx-B for 5 min each, slides were incubated with secondary antibodies for 1 h at RT in PBS-Tx-B. After washing three times in PBS, nuclei were stained with 2 μ g/mL Hoechst 33342 in PBS (Sigma Aldrich) and slides were mounted with DAKO mounting media (Agilent).

Spermatozoa (sarkosyl protocol) - Mouse sperm from caudae epididymides or human sperm from 250- μ L straws were collected in 1 mL PBS 1X, washed by centrifugation for 5 min at 500 g and then resuspended in 1 mL PBS 1X. Sperm cells were spread onto slides pre-coated with 0.1% poly-L-lysine (Epremedia), treated or not for 5 min with 0.2% sarkosyl (Sigma) in Tris-HCl 1 mM, pH7.5 at RT and then fixed in PBS/4% PFA for 45 s at RT. After washing twice for 5 min with PBS, sperm were permeabilized with PBS/0.1% Triton X-100 (Sigma Aldrich) for 15 min at RT and unspecific sites were blocked with PBS/0.1% Triton X-100/2% NGS for 30 min at RT. Then, sperm were incubated overnight at 4 °C with primary antibodies diluted in PBS/0.1% Triton X-100/2% NGS. Slides were washed three times with PBS/0.1% Triton X-100 before incubating with secondary antibody diluted in PBS/0.1% Triton X-100/2% NGS for 90 min at RT. Finally, sperm were washed three times in PBS/0.1% Triton X-100, adding 2 μ g/mL Hoechst 33342 (Sigma Aldrich) during the last wash to counterstain nuclei. Slides were mounted with DAKO mounting media (Agilent). Confocal microscopy was performed on a Zeiss LSM 710 or NIKON eclipse A1R/Ti2 using a 63x oil objective.

Image acquisition – For all immunofluorescence experiments, images were acquired using a 63X oil objective on a multimodal confocal Zeiss LSM 710 or Zeiss AxioObserver Z1 equipped with ApoTome and AxioCam MRm. Images were processed using Fiji (73) and Zeiss ZEN (Carl Zeiss, version 3.4). Figures for cultured cells were arranged using QuickFigures (74).

Expansion microscopy (U-ExM)

Coverslips used for either sample loading (12 mm) or image acquisition (24 mm) were first washed with absolute ethanol and dried. They were then coated with poly-D-lysine (0.1 mg/mL) for 1 h at 37 °C and washed three times with ddH₂O before use. Sperm from cauda epididymides or human sperm from straws were washed twice in PBS. 1×10^6 sperm cells were spun onto 12-mm coverslips for 3 min at 300 g. Crosslinking was performed in 1 mL of PBS/1.4% formaldehyde/2% acrylamide (ThermoFisher) for 5 h at 37 °C in a wet incubator. Cells were embedded in a gel by placing a 35- μ L drop of a monomer solution consisting of PBS/19% sodium acrylate/10% acrylamide/0.1% N,N'-methylenebisacrylamide/0.2% TEMED/0.2% APS (ThermoFisher) on parafilm and carefully placing coverslips on the drop, with sperm facing the gelling solution. Gelation proceeded in two steps: 5 min on ice followed by 1 h at 37 °C. Coverslips with attached gels were transferred into a 6-well plate for incubation in 5 mL of denaturation buffer (200 mM SDS, 200 mM NaCl, 50 mM Tris in ddH₂O, pH 9) for 20 min at RT until gels detached. Then, gels were transferred to a 1.5-mL microtube filled with fresh denaturation buffer and incubated for 90 min at 95 °C. Gels were carefully removed with tweezers and placed in beakers filled with 10 mL ddH₂O to cause expansion. The water was exchanged at least twice every 30 min. Finally, gels were incubated in 10 mL of ddH₂O overnight at RT. The following day, a 5-mm piece of gel was cut out with a punch. To remove excess water, gels were placed in 10 mL PBS for 15 min, the

buffer was changed, and incubation repeated once. Subsequently, gels were transferred to a 24-well plate and incubated with 300 μ L of primary antibody diluted in PBS/2% BSA at 37 °C for 3 h with vigorous shaking. After three washes for 10 min in PBS/0.1% Tween 20 (PBS-T) under agitation, gels were incubated with 300 μ L of secondary antibody in PBS/2% BSA at 37 °C for 3 h with vigorous shaking. Finally, gels were washed three times in PBS-T for 10 min with agitation. Hoechst 33342 (2 μ g/mL) was added during the last wash. The expansion resolution was between 4X and 4.2X depending on sodium acrylate purity. For image acquisition, gels were placed in beakers filled with 10 mL ddH₂O. Water was exchanged at least twice every 30 min, and then expanded gels were mounted on 24-mm round poly-D-lysine-coated coverslips, placed in a 36-mm metallic chamber for imaging. Confocal microscopy was performed using either a Zeiss LSM 710 using a 63x oil objective or widefield was performed using a Leica THUNDER widefield fluorescence microscope, using a 63x oil objective and small volume computational clearing. (Guichard / Hamel lab, Geneva).

***Ccdc146* expression**

Testis from CCDC146-HA pups were collected at days 9, 18, 26 and 35 after birth and directly cryopreserved at -80 °C before RNA extraction. RNA was extracted as follow. Frozen testes were placed in RLT buffer (Qiagen)/1% β -mercaptoethanol (Sigma), cut in small pieces and lysis performed for 30 min at RT. After addition of 10 volumes of TRIzol (5 min, RT, ThermoFisher) and 1 volume of chloroform (2 min, RT, Sigma Aldrich), the aqueous phase was recovered after centrifugation at 12 000 g, 15 min, 4 °C. RNA was precipitated by the addition of one volume of isopropanol (Sigma) and of glycogen (20 mg/mL, ThermoFisher) as a carrier, tube was placed overnight at -20 °C. The day after, after centrifugation (15 min, 12 000 g, 4 °C), RNA pellet was washed with ethanol 80%, air-dried and resuspended in 30 μ L of ultrapure RNase free water (Gibco). RNA concentrations were determined by using the Qubit RNA assay kit (ThermoFisher). 800 ng of total RNA were used to perform the RT step using the iScript cDNA synthesis kit (Bio-Rad) in a total volume of 20 μ L. Gene expression was assessed by qPCR (1 μ L of undiluted cDNA in a final volume of 20 μ L with the appropriate amount of primers, see table 1) using the SsoAdvanced Universal SYBR Green Supermix (Bio-Rad). The qPCR program used was 94 °C 15 min, (94 °C 30 s, 58 °C 30 s, 72 °C 30 s) x40 followed by a melt curve analysis (58 °C 0.05 s, 58–95 °C 0.5-°C increment 2–5 s/step). Gene expression was calculated using the 2^{-CT} method. Results are expressed relative to *Ccdc146* expression on day 9.

Genes	Forward primer		Reverse primer	
	Sequence	Concentration (nM)	Sequence	Concentration (nM)
<i>Ccdc146</i>	5'-TGCTGCATGACGCCGTGATG-3'	750	5'-GGAGACCTCCGTGGAGAATGCTTC-3'	500
<i>Hprt</i>	5'-CCTAATCATTATGCCGAGGATTTGG-3'	500	5'-TCCCATCTCCTTCATGACATCTCG-3'	250
<i>Actb</i>	5'-CTTCTTTGCAGCTCCTTCGTTGC-3'	250	5'-AGCCGTTGTCGACGACCAGC-3'	250

CCDC146 detection by WB

Protein extraction from the testis – Testis from pups were recovered at days 9, 18, 26 and 35 after birth. After removing the albuginea, they were homogenized in 2X Laemmli buffer (Bio-Rad) using a Dounce homogenizer, and heated at 95 °C for 10 min. The supernatant was recovered after centrifugation (15 000 g, 10 min, 4 °C), 5% β mercapto-ethanol was added (Sigma), and tubes were once again incubated at 95 °C for 10 min. After cooling, the supernatant was stored at -20 °C until use.

Protein extraction from sperm head and sperm flagella – Spermatozoa from a CCDC146-HA male (9 weeks old) were isolated from both epididymis in 1 mL PBS and washed twice with PBS by centrifugation at RT (5 min, 500 g). Half of the sperm were incubated with 1X protease inhibitor cocktail (mini Complete EDTA-free tablet, Roche Diagnostic), incubated for 15 min on ice and sonicated. Separated flagella were isolated by centrifugation (600 g, 20 min, 4 °C) in a Percoll gradient. Percoll concentrations used were 100%, 80%, 60%, 34%, 26%, 23%, and sperm flagella were isolated from the 60% fraction. Samples were washed with PBS by centrifugation (500 g, 10 min, 4 °C). Whole sperm or sperm flagella were incubated in 2X Laemmli buffer (Bio-Rad), heated at 95 °C for 10 min and centrifuged (15 000 g, 10 min, 4 °C). The supernatants were incubated with 5% β-mercaptoethanol, boiled (95 °C, 10 min), cooled down and placed at -20 °C until use.

Proteins extraction from total sperm – CCDC146-HA sperm were recovered from caudae epididymides in 1 mL PBS and washed twice in 1 mL PBS by centrifugation 500 g, 5 min. Lysis was then performed for 2 h at 4 °C on wheel in either Chaps buffer (10 mM Chaps / 10 mM HEPES / 137 mM NaCl / 10% Glycerol), in RIPA Buffer (Pierce IP Lysis buffer, ThermoFisher), in Tris 10 mM / HCl 1 M buffer or in Tris 10 mM / HCl 1 M / 0.2 to 0.8% sarkosyl buffer. After centrifugation 15 000 g, 4 °C, 15 min, the supernatants were recovered and 5% of β-mercaptoethanol added. After boiling (95 °C, 10 min), the samples were cooled down and placed at -20 °C until use.

Western blot – Protein lysates were fractionated on 5-12% SDS-PAGE precast gels (Bio-Rad) and transferred onto Trans-Blot Turbo Mini 0.2 µm PVDF membranes using the Trans-Blot Turbo Transfer System (Bio-Rad) and the appropriate program. Membranes were then blocked in PBS/5% milk/0.1% Tween 20 (PBS-T) for 2 h at RT before incubating with the primary antibody in PBS-T overnight at 4 °C with agitation. Membranes were then washed three times for 5 min in PBS-T and incubated with the secondary HRP-antibody in PBS-T for 1 h at RT. After three washes (PBS-T, 10 min), the membrane was revealed by chemiluminescence using the Clarity ECL substrate (Bio-Rad) and images were acquired on a Chemidoc apparatus (Bio-Rad).

Transmission electron microscopy

Transmission electron microscopy was performed by Dr. Stefan Geimer at the University of Bayreuth as follows. Testis from adult mice were fixed in PBS/4% paraformaldehyde (PFA). They were then decapsulated from the tunica albuginea and the seminiferous tubules were divided into three to four pieces using a razor blade (Gillette Super Shaver). The seminiferous tubules were incubated for 60 min at RT in fixation buffer (100 mM HEPES pH7.4, 4 mM CaCl₂, 2.5% glutaraldehyde, 2% PFA, all from Sigma Aldrich) and then the buffer was exchanged with fresh fixation buffer and the samples left overnight fixed at 4 °C. After washing three times for 10 min in 100 mM HEPES pH 7.4, 4 mM CaCl₂, samples were post-fixed in 1% osmium tetroxide (Carl Roth, Karlsruhe, DE) in distilled water for 120 min at 4 °C. After three additional 10-min washes in distilled water, the tissue pieces were embedded in 1.5% Difco™ Agar noble (Becton, Dickinson and Company, Sparks, MD, US) and dehydrated using increasing concentrations of ethanol. The samples were then embedded in glycidyl ether 100 (formerly Epon 812; Serva, Heidelberg, Germany) using propylene oxide as an intermediate solvent according to the standard procedure. Ultrathin sections (60-80 nm) were cut with a diamond knife (type ultra 35°; Diatome, Biel, CH) on the EM UC6 ultramicrotome (Leica Microsystems, Wetzlar, Germany) and mounted on single-slot pioloform-coated copper grids (Plano, Wetzlar, Germany). Finally, sections were stained with uranyl acetate and lead citrate (75). To obtain different section planes within a sample, serial sections (60-80 nm) were made using the same method. The sectioned and contrasted samples were analyzed under a JEM-2100 transmission electron microscope (JEOL, Tokyo, JP) at an acceleration voltage of 80 kV. Images were acquired using a 4080 x 4080 charge-coupled device camera (UltraScan 4000 - Gatan, Pleasanton, CA, US) and Gatan Digital Micrograph software. The brightness and contrast of images were adjusted using the ImageJ program.

Scanning electron microscopy

The two epididymides of mature males were recovered in 1 mL of 0.1 M sodium cacodylate buffer (pH 7.4, Electron Microscopy Sciences) and the sperm were allowed to swim for 15 min at 37 °C. After centrifugation for 10 min, 400 g, RT, the supernatant was discarded and the pellet resuspended in primary fixating buffer (2% glutaraldehyde/0.1 M sodium cacodylate buffer, pH 7.4, Electron Microscopy Sciences) for 30 min at 4 °C. After washing three times in 0.1 M sodium cacodylate buffer (400 g, 10 min), the pellet was submitted to post fixation using 1% Osmium tetroxide 2% (OsO₄, Electron Microscopy Sciences) in 0.1 M sodium cacodylate buffer for 30 min at 4 °C. Fixed cells were washed three times in 0.1 M sodium cacodylate buffer (400 g, 5 min), the sample was then placed on a coverslip and treated with Alcian blue 1% (Electron Microscopy Sciences) to improve attachment. The sample was then dehydrated in graded ethanol series: 50%, 70%, 80%, 90%, 96% and 100% (10 min, once each). Final dehydration was performed for 10 min in a v/v solution of 100% ethanol/100% Hexamethyldisilazane (HMDS) followed by 10 min in 100% HMDS. Samples were left to dry overnight before performing metallization. Samples were analyzed using a

Zeiss Ultra 55 microscope at the C.M.T.C. – Consortium des Moyens Technologiques Communs (Material characterization platform), Grenoble INP.

Statistical analysis

The statistics related to the reproductive phenotypes were automatically calculated by GraphPad Prism 8 and 9. Statistical differences were assessed by applying an unpaired t test and one-way ANOVA. Histograms show mean \pm standard deviation, and p-values were considered significant when inferior to 0.05.

Antibodies used

Primary antibodies				
Target	Host species	Reference		Dilution
CCDC146	Rabbit	Atlas Antibodies	HPA020082	IF: 1/200 U-ExM: 1/200
Centrin, 20H5	Mouse	Merck	04-1624	IF: 1/200
γ -tubulin	Mouse	Santa Cruz Biotechnology	sc-17787	IF: 1/500
β -tubulin	Guinea pig	Geneva Antibody Facility	AA344-GP	IF: 1/500
β -tubulin	Rabbit	Cell Signaling Technology	2128	IF: 1/100
PCM1 (G-6)	Mouse	Santa Cruz Biotechnology	sc-398365	IF: 1/200
α -tubulin	Mouse	Geneva Antibody Facility	AA-345	U-ExM: 1/250
β -tubulin *			AA-344	IF: 1/500
POC5	Rabbit	Bethyl	A303-341A	IF: 1/250 U-ExM: 1/200
High Affinity (HA)	Rat	Roche	11867423001	IF: 1/400

				U-ExM: 1/400 WB: 1/2500
High Affinity (HA)	Rabbit	Cell Signaling Technology	3724	U-ExM: 1/100
High Affinity (HA)	Rabbit	Sigma Aldrich	H6908	U-ExM: 1/200
Dpy19L2	Rabbit	**		IF: 1/100

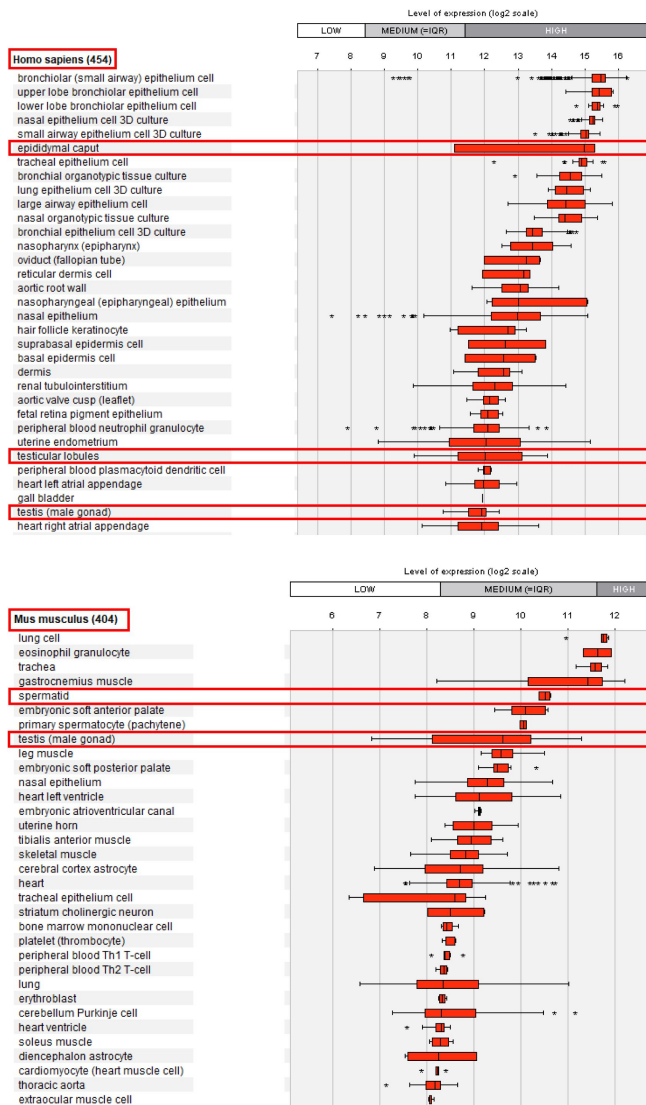
Target	Fluorophore	Reference		Dilution
Goat anti-Rabbit	Alexa Fluor 488	Jackson ImmunoResearch	111-545-144	IF: 1/800 U-ExM: 1/250
Goat anti-Mouse	DyLight 549	Jackson ImmunoResearch	115-505-062	IF: 1/400
Goat anti-Guinea Pig	Alexa Fluor 647	Invitrogen	A-21450	IF: 1/800
Goat anti-Rabbit	Alexa Fluor 568	Life Technologies	A11036	U-ExM: 1/250
Goat anti-Mouse	Alexa Fluor 488	Life Technologies	A11029	U-ExM: 1/250
Goat anti-Rat	Alexa Fluor 549	Jackson ImmunoResearch	112-505-175	IF: 1/800
Goat Anti-Rat	HRP conjugate	Merck	AP136P	1/10 000

* α -tubulin and β -tubulin were used together and noted as α + β -tubulin

**Dpy19L2 antibodies are polyclonal antibodies produced in rabbit that were raised against RSKLREGSSDRPQSSC and CTGQARRRWSAATMEP peptides corresponding to amino acids 6-21 and 21-36 of the N-terminus of mouse Dpy19L2, as described in [76].

Acknowledgements

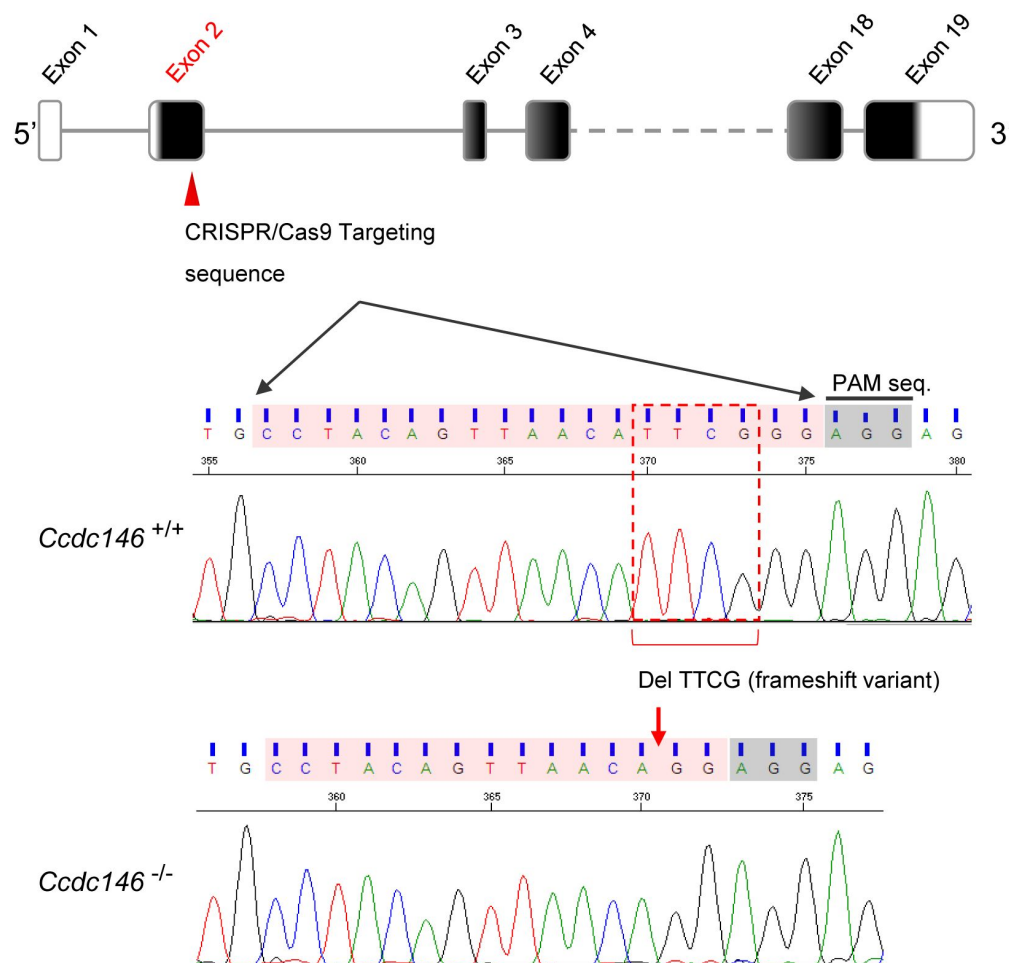
This work was supported by INSERM, CNRS, Université Grenoble Alpes, the French Agence Nationale pour la Recherche (ANR) grants “MAS-Flagella” (ANR-19-CE17-0014), and “FLAGELOME” (ANR-19-CE17-0014) to P.F.R., the Direction Générale de l’Offre de Soins (DGOS) for the program PRTS 2014 to P.F.R., the Fondation Maladies Rares (FMR)- grant “Whole genome sequencing of subjects with Flagellar Growth Defects (FGD)” financed by for the program Séquençage à haut débit 2012 to P.F.R. and the European Research Council (ERC) ACCENT Starting Grant 715289 to P.G.



Appendix-Figure 1.

Relative mRNA expression levels for human and mouse CDC146 transcripts.

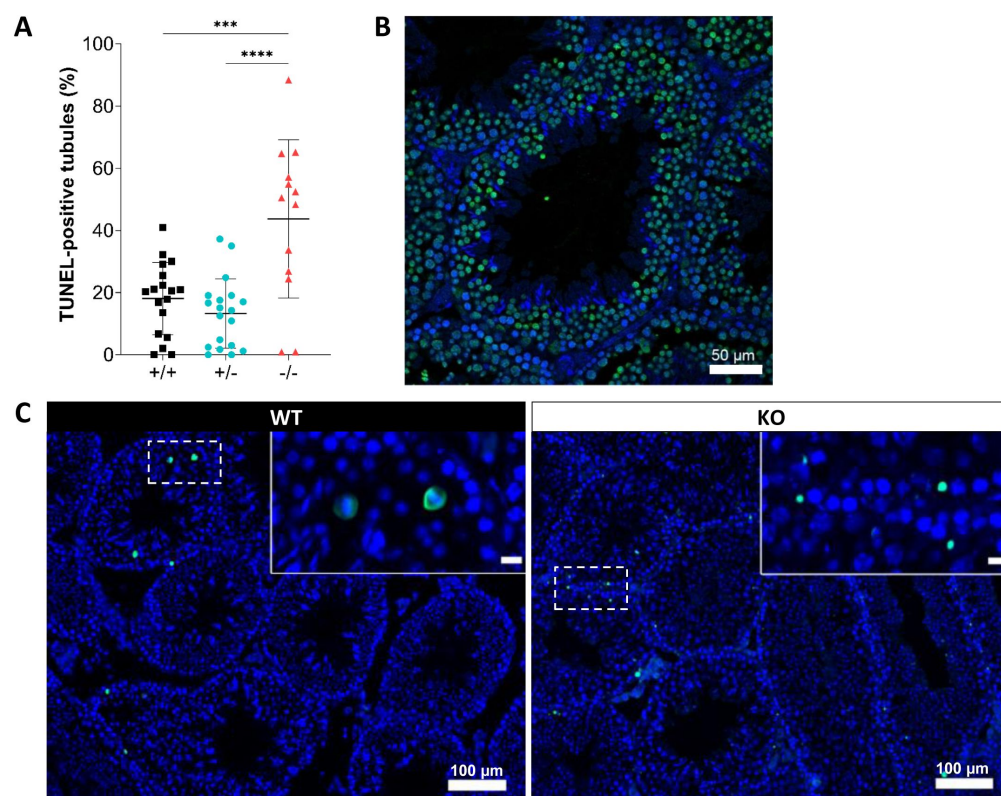
(A) CDC146 mRNA levels measured in different tissues/cells in humans using Affymetrix microarrays (data available from the Genevestigator database, <https://genevestigator.com>). Red rectangles highlight the high expression level in male reproductive organs. (B) Similar data for mice. Data were generated with Genevestigator (Hruz T, Laule O, Szabo G, Wessendorp F, Bleuler S, Oertle L, Widmayer P, Gruissem W and P Zimmermann (2008) Genevestigator V3: a reference expression database for the meta-analysis of transcriptomes. *Advances in Bioinformatics* 2008, 420747)



Appendix-Figure 2.

Molecular strategy used to generate *Ccdc146* KO mice by CRISPR/Cas9

The exonic structure of mouse *Ccdc146* is shown and the coding sequence indicated in black. Exon 2, the first coding sequence, was targeted by an RNA guide (5'-CCT ACA GTT AAC ATT CGG G-3) and the Cas9 induced a deletion of four nucleotides upstream the PAM sequence, as indicated by the red box. Electropherogram presenting the WT and the homozygote deletion are shown.

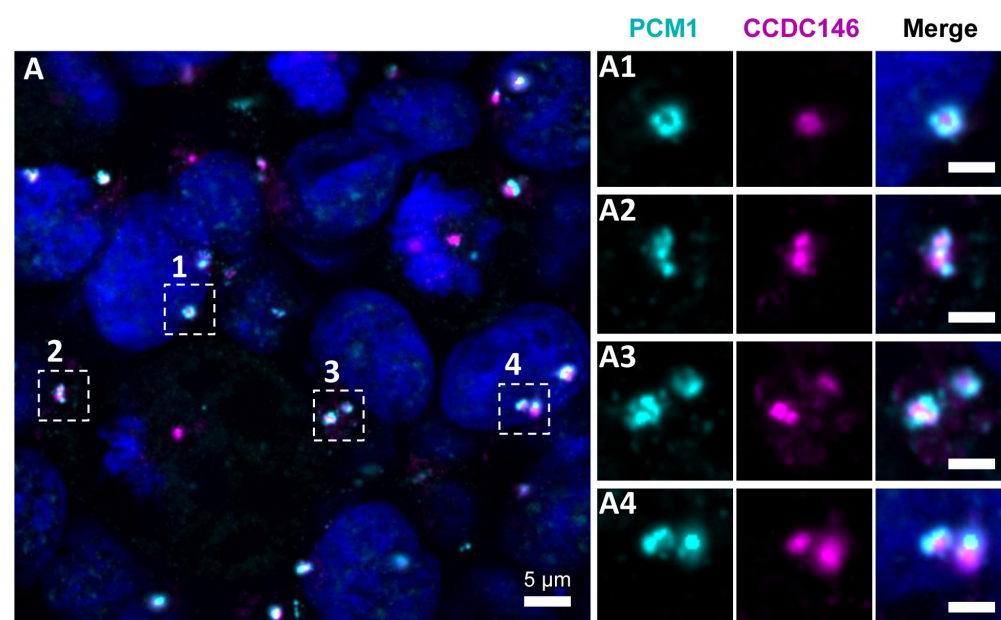


pachytene cells undergoing meiosis (B, WT zoomed image) whereas the localization of TUNEL-positive cells in KO was more scattered. (C) Control testis section treated with H2O2. Statistical comparisons according to ordinary one-way ANOVA test (**** $p < 0.0001$; *** $p < 0.001$, ** $p < 0.01$, * $p < 0.05$). Scale bar of zoomed images 50 μ m.

Appendix-Figure 3.

Increased levels of apoptosis in testes from *Ccdc146* KO mice.

The TUNEL assay was used to visualize double-strand DNA breaks, as an indication of the level of apoptosis during WT and KO spermatogenesis. (A) Comparison of the % of tubules per testis cross-section containing at least one TUNEL-positive cell in WT, heterozygote, and *Ccdc146* KO animals. Number of sections counted per genotype $n = 13-20$, 3 different mice per genotype. (B) The majority of TUNEL-positive cells in the WT corresponded to

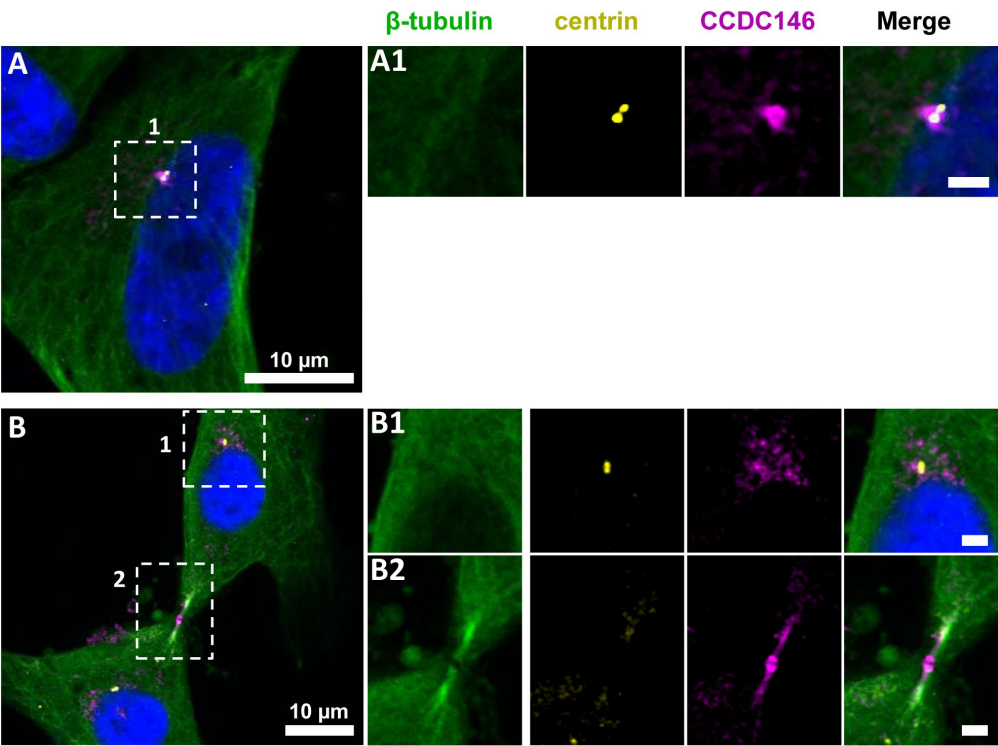


Appendix-Figure 4.

CCDC146 does not colocalize with the centriolar satellite marker PCM1.

(A) HEK-293T cells were double immunolabeled for PCM1 (cyan) and CCDC146 (magenta). (A1-A4) Images on the right show the enlargement of the dotted squares in the left image. PCM1 surrounds the CCDC146 signal, but no colocalization is observed, suggesting that CCDC146 is not a centriolar satellite pro-

tein. DNA was stained with Hoechst (blue). Scale bars on zoomed images represent 2 μ m.



Appendix-Figure 5.

CCDC146 shows a similar localization to the centrosome and to the midbody in primary HFF cells.

(A) Primary human foreskin fibroblast (HFF) cells were triple immunolabeled with anti-β-tubulin (green), anti-centrin (yellow, showing the centrosomes) and anti-CCDC146 (magenta). (A1) The right-hand images show the enlargement of the dotted squares in the left-hand image. CCDC146 localized to and around the centrosomes. (B) similar staining showing co-labeling of the midbody during cytokinesis by anti-CCDC146 Abs (B2). Scale bar of zoomed images 2 μm.

ing showing co-labeling of the midbody during cytokinesis by anti-CCDC146 Abs (B2). Scale bar of zoomed images 2 μm.

Ccdc146 : Knock-in Edits

Transcript: ENSMUST00000115245.7 (GRCm38.p6)

Guide RNA design

TAC TTT AGA ACT GTG AAAA **ATGG** (in red, the start codon in exon 2/19)

HA Tag sequence

Coding sequence (5'-3') : **TAC CCA TAC GAT GTT CCA GAT TAC GCT**

Amino-acid sequence (N-C ter) : Y P Y D V P D Y A

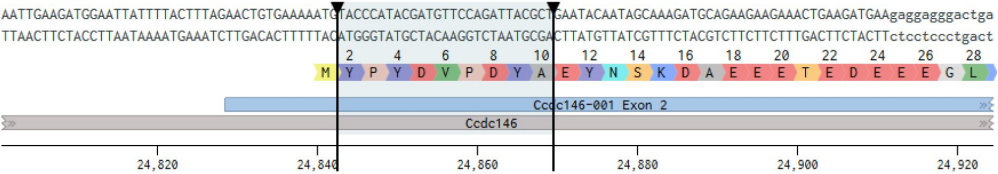
Appendix-Figure 6.

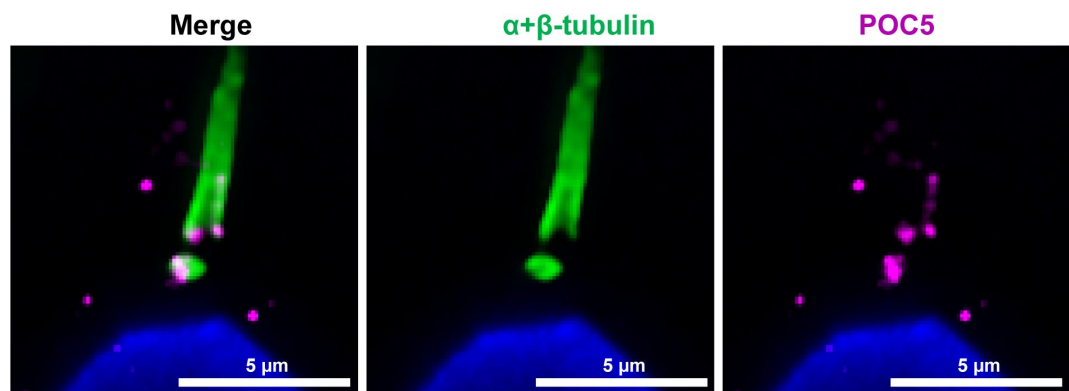
Molecular strategy used to generate HA-tagged CCDC146 mice by CRISPR/Cas9

The reference CCDC146 mouse transcript is ENSMUST00000115245.7 (GRCm38.p6). Exon 2, the first coding sequence, was targeted by an RNA guide (5'- TAC TTT AGA ACT GTG AAA AAT GG -3'). We used a single-stranded DNA (ss-DNA) template to insert the HA sequence (5'-TAC CCA TAC GAT GTT CCA GAT TAC GCT-3') upstream of the PAM sequence.

Strand	Sequence	PAM	On-target score	Off-target score
+	TAC TTT AGA ACT GTG AAAA A	TGG	27.9	29.0

1) Tag insertion :

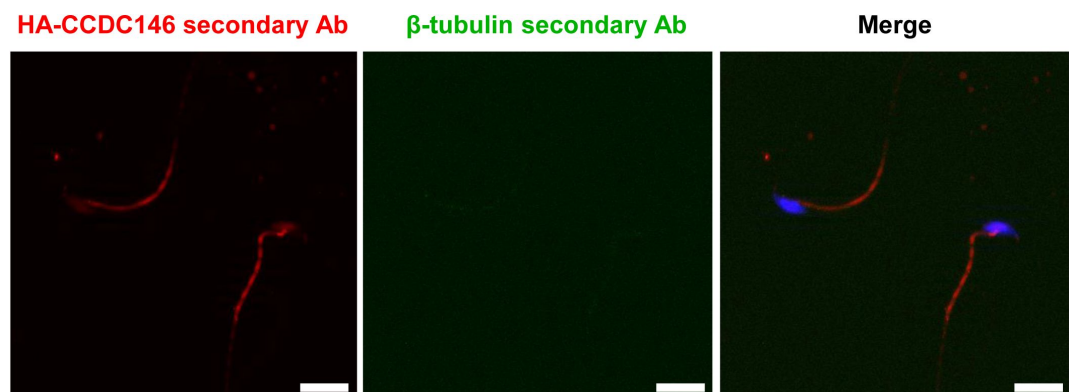




Appendix-Figure 7.

Centrioles are identified by anti-POC5 Abs in expanded human ejaculated spermatozoa.

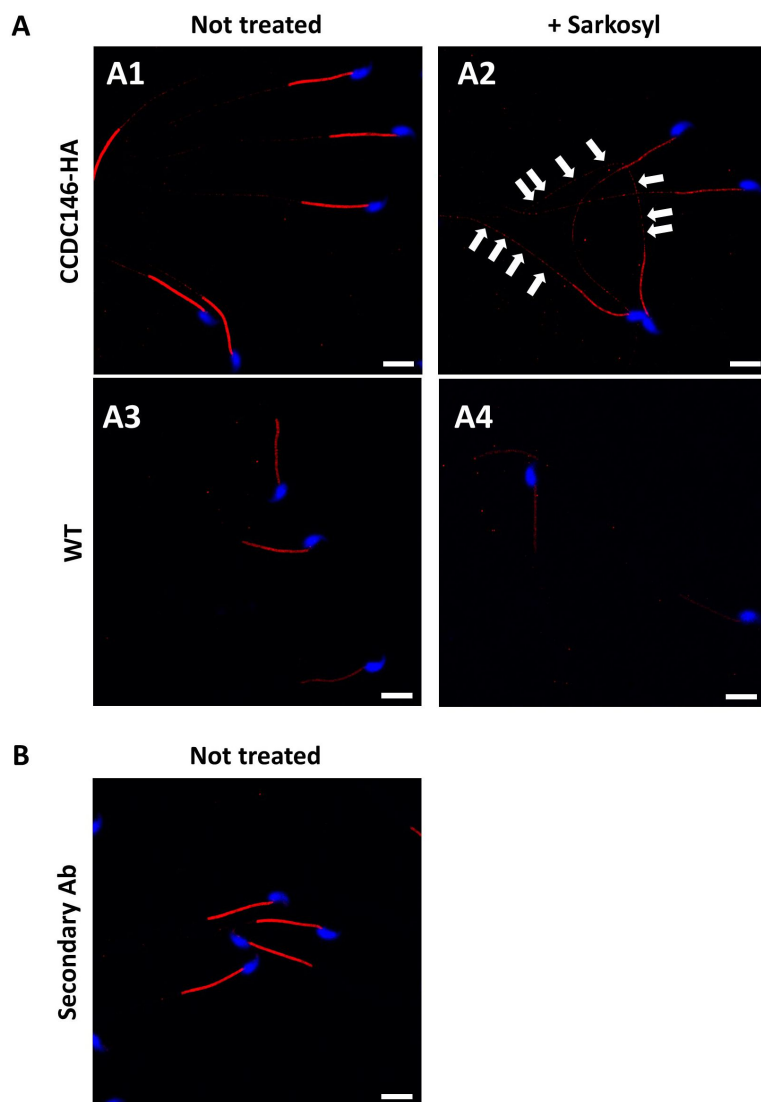
Human control sperm were co-stained, after expansion, with anti- α + β -tubulin (green) and anti-POC5 (magenta) Abs. The centrosomal protein POC5 locates to centrioles at the base of the axoneme. Scale bars 5 μ m.



Appendix-Figure 8.

Non-specific midpiece staining in mouse sperm by rabbit secondary antibody.

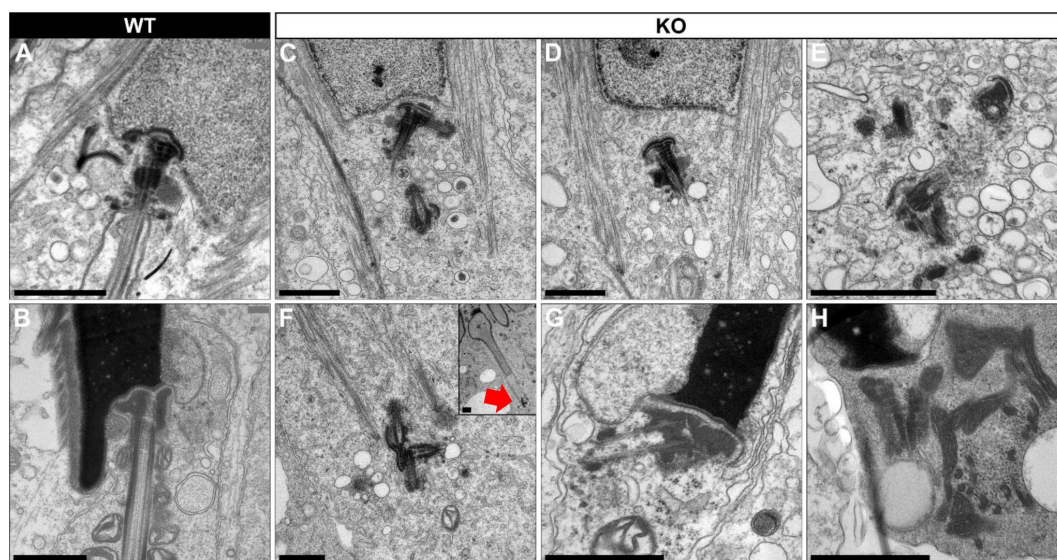
Mouse sperm were stained with secondary antibodies only. Scale bars 10 μ m.



Appendix—Figure 9.

Sperm sarkosyl treatment corroborates the presence of CCDC146 along the mouse flagellum.

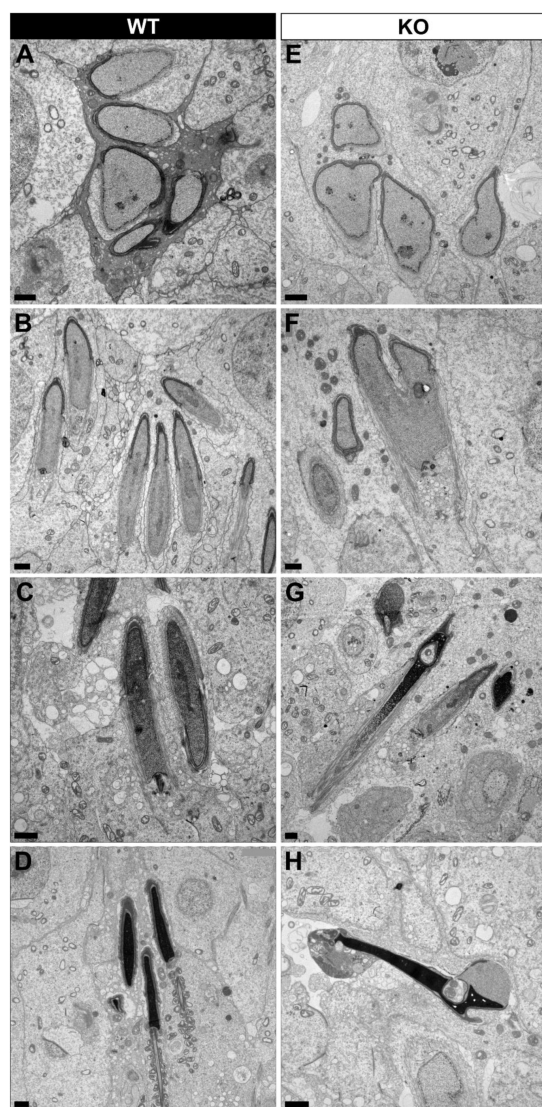
CCDC146-HA sperm (A1-A2) and epididymal WT (A3-A4) not treated or treated (5 min, 0.2% sarkosyl), were immunostained with anti-HA Ab (red) and counterstained with Hoechst (blue). (A1) Without treatment, a faint CCDC146-HA signal was observed along the CCDC146-HA principal piece. The strong staining in the midpiece is not specific (see panel B) (A2) After treatment with sarkosyl, the CCDC146- HA signal along the sperm principal piece was enhanced (white arrows), whereas the signal in the midpiece decreased. (A3) WT untreated (NT) sperm exhibited almost no CCDC146-HA signal in the principal piece. The midpiece is however strongly stained (not specific see panel B) (A4) The HA signal is not enhanced in WT principal piece by sarkosyl treatment, suggesting that the enhanced signal observed with sarkosyl on CCDC146-HA sperm is specific. (B) CCDC146-HA sperm were immunolabeled with secondary antibody only. Strong staining is observed on the midpiece, confirming its non-specific nature. Scale bars 10 μ m.



Appendix-Figure 10.

Lack of CCDC146 causes centriole duplication and mislocalization in *Ccdc146* KO spermatids.

Ultrastructural analysis of centrioles in adult mouse WT (A, B) and *Ccdc146* KO (C-H) testis sections. (A) In WT spermatids, the proximal centriole is linked to the base of the compacting nucleus through the basal plate and the capitulum, and the distal centriole is embedded in the segmented column. These sperm-specific cytoskeletal structures make up the head-to-tail coupling apparatus (HTCA). (B) In WT elongated spermatids, the different components of the axonemal structures (microtubules and ODF) were visible downstream the distal centriole. (C) In *Ccdc146* KO elongating spermatids, the overall structure of the HTCA was conserved, with the presence of the centrioles and the accessory cytoskeletal structures. However, the HTCAs were often duplicated (C, E, F) and separated from their usual nuclear attachment site (C-F, H), and sometimes misplaced far away from the nucleus (F), likely preventing axoneme elongation. (F) The arrow indicates the misplaced centrioles at the end of the manchette. (G, H) In elongated spermatids with condensed nucleus, malformed and detached centrioles with poorly-assembled or missing flagella compared to the WT (B) can be seen.



Appendix-Figure 11.

Spermatid head shape is aberrant in the absence of CCDC146.

Comparative ultrastructural analysis of the spermatid head in WT (A-D) and *Ccdc146* KO (E-H) testis sections. (A, E) Spermatid nuclei at the beginning of elongation. KO spermatid nuclei showing nuclear membrane invaginations and irregular shape that were not present in the WT. The acrosome in the KO sperm appeared intact. (B, F) Spermatid nuclei in elongating spermatids. Whereas nucleus elongation is symmetric in the WT, in the *CCDC146*-KO, more pronounced head invaginations are observed. (C, G) Elongated spermatids. Although nuclear condensation appeared normal in both WT and KO nuclei, vacuolization is observed in KO nucleus. (D, H) Elongated KO spermatids showed malformed elongated nuclear shapes with frequent invaginations and poorly-assembled flagella (H) compared to the WT (D).

Table Supplementary 1

List of primers used for Sanger verification of the identified variants by WES.

Primer name	Primer sequence (5'-3')	Tm (°C)	Product length (bp)
CCDC146-Int8F	ATTGCTGGGTCAAACGGTAG	57.3	422
CCDC146-Int9R	GGCAGCAAAAACAACCTTCCT	55.3	
CCDC146-Ex15F	CAGCTGATAGAGCGGGAAGA	59.3	457
CCDC146-Int15R	TCCAAGAAAAGCAGAAAATGC	54.0	

List of primers used for knock-out mice genotyping.

Primer name	Primer sequence (5'-3')	Tm (°C)	Product length (bp)
Ccdc146-Ex2F3	GGGAGGAACAGGAGAAGGAG	61.4	151
Ccdc146-Ex2R3	TCATGCAGACAGAGGAAAGC	57.3	

List of primers used for knock-in mice (HA-Tag) genotyping.

Primer name	Primer sequence (5'-3')	Tm (°C)	Product length (bp)
shCCD_ki-F1	ACTTGGTGGGTGTTGTCTTA	58.49	149
shCCD_ki-R1	TCCCTCCTCTTCATCTTCAGT	57.52	
IgCCD_ki-F1	AGAAATCAGGGAGGGGTTGC	59.67	504
IgCCD_ki-R1	AATTGATGAGCCGCTCCTCC	60.18	

References

- Boivin J. (2007) **International estimates of infertility prevalence and treatment-seeking: potential need and demand for infertility medical care** **22**:1506–1512
- Uhlén M. (2016) **Transcriptomics resources of human tissues and organs** **12**:862
- Houston B.J. (2021) **A systematic review of the validated monogenic causes of human male infertility: 2020 update and a discussion of emerging gene-disease relationships** **28**:15–29
- Beurois J. (2020) **Genetics of teratozoospermia: Back to the head** **34**:101473
- Touré A. (2021) **The genetic architecture of morphological abnormalities of the sperm tail** **140**:21–42
- Wang J. (2022) **Clinical detection, diagnosis and treatment of morphological abnormalities of sperm flagella: A review of literature** *Front Genet* **13**:1034951

7. Sironen A. (2020) **Sperm defects in primary ciliary dyskinesia and related causes of male infertility** *77*:2029–2048
8. Lores P. (2018) **Homozygous missense mutation L673P in adenylate kinase 7 (AK7) leads to primary male infertility and multiple morphological anomalies of the flagella but not to primary ciliary dyskinesia** *Hum Mol Genet*
9. Coutton C. (2019) **Bi-allelic Mutations in ARMC2 Lead to Severe Astheno-Teratozoospermia Due to Sperm Flagellum Malformations in Humans and Mice** *104*:331–340
10. Shen Q. (2021) **Bi-allelic truncating variants in CFAP206 cause male infertility in human and mouse** *140*:1367–1377
11. Cong J. (2022) **Homozygous mutations in CCDC34 cause male infertility with oligoasthenoteratozoospermia in humans and mice** *59*:710–718
12. Kherraf Z.E. (2018) **A Homozygous Ancestral SVA-Insertion-Mediated Deletion in WDR66 Induces Multiple Morphological Abnormalities of the Sperm Flagellum and Male Infertility** *103*:400–412
13. Coutton C. (2018) **Mutations in CFAP43 and CFAP44 cause male infertility and flagellum defects in Trypanosoma and human** *9*:686
14. Liu C. (2021) **Deleterious variants in X-linked CFAP47 induce asthenoteratozoospermia and primary male infertility** *108*:309–323
15. Liu S. (2021) **CFAP61 is required for sperm flagellum formation and male fertility in human and mouse** *148*:
16. Li W. (2020) **Biallelic mutations in CFAP65 cause male infertility with multiple morphological abnormalities of the sperm flagella in humans and mice** *57*:89–95
17. Dong F.N. (2018) **Absence of CFAP69 Causes Male Infertility due to Multiple Morphological Abnormalities of the Flagella in Human and Mouse** *102*:636–648
18. Beurois J. (2019) **CFAP70 mutations lead to male infertility due to severe asthenoteratozoospermia. A case report** *34*:2071–2079
19. Martinez G. (2020) **Biallelic variants in MAATS1 encoding CFAP91, a calmodulin-associated and spoke-associated complex protein, cause severe asthenoteratozoospermia and male infertility** *57*:708–716
20. Khelifa Ben , et al M. (2014) **Mutations in DNAH1, which encodes an inner arm heavy chain dynein, lead to male infertility from multiple morphological abnormalities of the sperm flagella** *94*:95–104
21. Liu C. (2020) **Bi-allelic DNAH8 Variants Lead to Multiple Morphological Abnormalities of the Sperm Flagella and Primary Male Infertility** *107*:330–341

22. Martinez G. (2018) **Whole-exome sequencing identifies mutations in FSIP2 as a recurrent cause of multiple morphological abnormalities of the sperm flagella** 33:1973–1984
23. Lorès P. (2021) **A missense mutation in IFT74, encoding for an essential component for intraflagellar transport of Tubulin, causes asthenozoospermia and male infertility without clinical signs of Bardet-Biedl syndrome** 140:1031–1043
24. Kherraf Z.E. (2019) **Whole exome sequencing of men with multiple morphological abnormalities of the sperm flagella reveals novel homozygous QRICH2 mutations** 96:394–401
25. Liu C. (2020) **Homozygous mutations in SPEF2 induce multiple morphological abnormalities of the sperm flagella and male infertility** 57:31–37
26. Liu W. (2019) **Bi-allelic Mutations in TTC21A Induce Asthenoteratospermia in Humans and Mice** 104:738–748
27. Lorès P. (2019) **Mutations in TTC29, Encoding an Evolutionarily Conserved Axonemal Protein, Result in Asthenozoospermia and Male Infertility** 105:1148–1167
28. Firat-Karalar E.N. (2014) **Proteomic analysis of mammalian sperm cells identifies new components of the centrosome** 127:4128–4133
29. Almeida F. (2018) **The Human Centrosomal Protein CCDC146 Binds Chlamydia trachomatis Inclusion Membrane Protein CT288 and Is Recruited to the Periphery of the Chlamydia- Containing Vacuole** *Front Cell Infect Microbiol* 8:
30. Blanco-Ameijeiras J. , Lozano-Fernández P. , Martí E. (2022) **Centrosome maturation - in tune with the cell cycle** *J Cell Sci* 135:
31. Wu B. (2020) **The coupling apparatus of the sperm head and tail†** 102:988–998
32. Fishman E.L. (2018) **A novel atypical sperm centriole is functional during human fertilization** 9:2210
33. Manandhar G. (1998) **Centrosome reduction during mouse spermiogenesis** 203:424–434
34. Sha Y.W. (2017) **A homozygous CEP135 mutation is associated with multiple morphological abnormalities of the sperm flagella (MMAF)** *Gene* 633:48–53
35. Zhang X. (2022) **CEP128 is involved in spermatogenesis in humans and mice** 13:1395
36. Lv M. (2020) **Homozygous mutations in DZIP1 can induce asthenoteratospermia with severe MMAF** 57:445–453

37. Sha Y. (2021) **Biallelic mutations of CFAP58 are associated with multiple morphological abnormalities of the sperm flagella** 99:443–448
38. Zhu Z.J. (2022) **Novel mutation in ODF2 causes multiple morphological abnormalities of the sperm flagella in an infertile male** 24:463–472
39. Nakagawa Y. (2001) **Outer dense fiber 2 is a widespread centrosome scaffold component preferentially associated with mother centrioles: its identification from isolated centrosomes** 12:1687–1697
40. Hall E.A. (2013) **Acute versus chronic loss of mammalian Azi1/Cep131 results in distinct ciliary phenotypes** 9:
41. Pasek R.C. (2016) **Coiled-coil domain containing 42 (Ccdc42) is necessary for proper sperm development and male fertility in the mouse** 412:208–18
42. Kherraf Z.E. (2022) **Whole-exome sequencing improves the diagnosis and care of men with non-obstructive azoospermia** 109:508–517
43. Odabasi E. , Batman U. , Firat-Karalar E.N. (2020) **Unraveling the mysteries of centriolar satellites: time to rewrite the textbooks about the centrosome/cilium complex** 31:866–872
44. Zindy F. (2001) **Control of spermatogenesis in mice by the cyclin D-dependent kinase inhibitors p18(Ink4c) and p19(Ink4d)** 21:3244–55
45. Gambarotto D. (2019) **Imaging cellular ultrastructures using expansion microscopy (U-ExM)** 16:71–74
46. Yanagisawa H.A. (2014) **FAP20 is an inner junction protein of doublet microtubules essential for both the planar asymmetrical waveform and stability of flagella in Chlamydomonas** 25:1472–83
47. Witman G.B. (1972) **Chlamydomonas flagella. I. Isolation and electrophoretic analysis of microtubules, matrix, membranes, and mastigonemes** 54:507–39
48. Linck R.W (1976) **Flagellar doublet microtubules: fractionation of minor components and alpha- tubulin from specific regions of the A-tubule** 20:405–39
49. Kirima J. , Oiwa K. (2018) **Flagellar-associated Protein FAP85 Is a Microtubule Inner Protein That Stabilizes Microtubules** 43:1–14
50. Simerly C. (2016) **Post-Testicular Sperm Maturation: Centriole Pairs, Found in Upper Epididymis, are Destroyed Prior to Sperm’s Release at Ejaculation** *Sci Rep* 6:31816
51. Kierszenbaum A.L. (2004) **The acroplaxome is the docking site of Golgi-derived myosin Va/Rab27a/b- containing proacrosomal vesicles in wild-type and Hrb mutant mouse spermatids** 70:1400–1410

52. Martinez G. (2022) **Oligogenic heterozygous inheritance of sperm abnormalities in mouse** *Elife* **11**:
53. Collins S.A. , Walker W.T. , Lucas J.S. (2014) **Genetic Testing in the Diagnosis of Primary Ciliary Dyskinesia: State-of-the-Art and Future Perspectives** **3**:491–503
54. Shoemark A. , Ozerovitch L. , Wilson R. (2007) **Aetiology in adult patients with bronchiectasis** **101**:1163–70
55. Li Z.Z. (2020) **The novel testicular enrichment protein Cfap58 is required for Notch-associated ciliogenesis** **40**:
56. Cuveillier C. (2021) **Beyond Neuronal Microtubule Stabilization: MAP6 and CRMP5, Two Converging Stories** *Front Mol Neurosci* **14**:665693
57. Ma M. (2019) **Structure of the Decorated Ciliary Doublet Microtubule** **179**:909–922
58. Jardin I. (2021) **SARAF and EFHB Modulate Store-Operated Ca(2+) Entry and Are Required for Cell Proliferation** **13**:
59. Segal R.A. (1984) **Mutant strains of Chlamydomonas reinhardtii that move backwards only** **98**:2026–34
60. Tam L.W. , Lefebvre P.A. (2002) **The Chlamydomonas MBO2 locus encodes a conserved coiled-coil protein important for flagellar waveform conversion** **51**:197–212
61. Shi Z. (2021) **Potential Novel Modules and Hub Genes as Prognostic Candidates of Thyroid Cancer by Weighted Gene Co-Expression Network Analysis** *Int J Gen Med* **14**:9433–9444
62. Kasak L. (2018) **Bi-allelic Recessive Loss-of-Function Variants in FANCM Cause Non-obstructive Azoospermia** **103**:200–212
63. Amargant F. (2021) **The human sperm basal body is a complex centrosome important for embryo preimplantation development** **27**:
64. Lehti M.S. , Sironen A. (2016) **Formation and function of the manchette and flagellum during spermatogenesis** **151**:–54
65. O'Donnell L. (2012) **An essential role for katanin p80 and microtubule severing in male gamete production** **8**:
66. Ho U.Y. (2021) **WDR62 is required for centriole duplication in spermatogenesis and manchette removal in spermiogenesis** **4**:645
67. Zhu F. (2016) **Biallelic SUN5 Mutations Cause Autosomal-Recessive Acephalic Spermatozoa Syndrome** **99**:942–949

68. Yuan S. (2015) **Spata6 is required for normal assembly of the sperm connecting piece and tight head-tail conjunction** 112:
69. Hoyer-Fender S (2022) **Development of the Connecting Piece in ODF1-Deficient Mouse Spermatids** 23:
70. Dunleavy J.E.M. (2017) **Katanin-like 2 (KATNAL2) functions in multiple aspects of haploid male germ cell development in the mouse** 13:
71. Giordano T. (2019) **Loss of the deglutamylase CCP5 perturbs multiple steps of spermatogenesis and leads to male infertility** 132:
72. Wang Y. (2014) **Variability in the morphologic assessment of human sperm: use of the strict criteria recommended by the World Health Organization in 2010** 101:945–9
73. Schindelin J. (2012) **Fiji: an open-source platform for biological-image analysis** 9:676–82
74. Mazo G. (2021) **QuickFigures: A toolkit and ImageJ PlugIn to quickly transform microscope images into scientific figures** 16:
75. Reynolds E.S (1963) **The use of lead citrate at high pH as an electron-opaque stain in electron microscopy** 17:208–12
76. Pierre V. (2012) **Absence of Dpy19l2, a new inner nuclear membrane protein, causes globozoospermia in mice by preventing the anchoring of the acrosome to the nucleus** 139:2955–65

Author information

1. Jana Muroňová

Institute for Advanced Biosciences, (IAB), INSERM 1209, Institute for Advanced Biosciences, (IAB) CNRS UMR 5309, Institute for Advanced Biosciences, (IAB) Université Grenoble Alpes

2. Zine-Eddine Kherraf

Institute for Advanced Biosciences, (IAB), INSERM 1209, Institute for Advanced Biosciences, (IAB) CNRS UMR 5309, Institute for Advanced Biosciences, (IAB) Université Grenoble Alpes, UM GI-DPI, CHU Grenoble Alpes, F-38000 Grenoble, France

3. Elsa Giordani

Institute for Advanced Biosciences, (IAB), INSERM 1209, Institute for Advanced Biosciences, (IAB) CNRS UMR 5309, Institute for Advanced Biosciences, (IAB) Université Grenoble Alpes

4. Simon Eckert

Cell Biology/ Electron Microscopy, University of Bayreuth, 95440 Bayreuth, Germany

5. Caroline Cazin

Institute for Advanced Biosciences, (IAB), INSERM 1209, Institute for Advanced Biosciences, (IAB) CNRS UMR 5309, Institute for Advanced Biosciences, (IAB) Université Grenoble Alpes, UM GI-DPI, CHU Grenoble Alpes, F-38000 Grenoble, France

6. Amir Amiri-Yekta

Institute for Advanced Biosciences, (IAB), INSERM 1209, Institute for Advanced Biosciences, (IAB) CNRS UMR 5309, Institute for Advanced Biosciences, (IAB) Université Grenoble Alpes, UM GI-DPI, CHU Grenoble Alpes, F-38000 Grenoble, France

7. Emeline Lambert

Institute for Advanced Biosciences, (IAB), INSERM 1209, Institute for Advanced Biosciences, (IAB) CNRS UMR 5309, Institute for Advanced Biosciences, (IAB) Université Grenoble Alpes

8. Geneviève Chevalier

Institute for Advanced Biosciences, (IAB), INSERM 1209, Institute for Advanced Biosciences, (IAB) CNRS UMR 5309, Institute for Advanced Biosciences, (IAB) Université Grenoble Alpes

9. Guillaume Martinez

Institute for Advanced Biosciences, (IAB), INSERM 1209, Institute for Advanced Biosciences, (IAB) CNRS UMR 5309, Institute for Advanced Biosciences, (IAB) Université Grenoble Alpes, UM de Génétique Chromosomique, Hôpital Couple-Enfant, CHU Grenoble Alpes, F-38000 Grenoble, France
ORCID iD: [0000-0002-7572-9096](https://orcid.org/0000-0002-7572-9096)

10. Yasmine Neirijnck

Department of Genetic Medicine and Development, University of Geneva Medical School, Geneva 1211, Switzerland

11. Françoise Kühne

Department of Genetic Medicine and Development, University of Geneva Medical School, Geneva 1211, Switzerland

12. Lydia Wehrli

Department of Genetic Medicine and Development, University of Geneva Medical School, Geneva 1211, Switzerland

13. Nikolai Klena

University of Geneva, Department of Molecular and Cellular Biology, Sciences III, Geneva, Switzerland, Human Technopole, 20157 Milan, Italy

14. Virginie Hamel

University of Geneva, Department of Molecular and Cellular Biology, Sciences III,
Geneva, Switzerland
ORCID iD: [0000-0001-5092-2343](https://orcid.org/0000-0001-5092-2343)

15. Jessica Escoffier

Institute for Advanced Biosciences, (IAB), INSERM 1209, Institute for Advanced
Biosciences, (IAB) CNRS UMR 5309, Institute for Advanced Biosciences, (IAB)
Université Grenoble Alpes
ORCID iD: [0000-0001-8166-5845](https://orcid.org/0000-0001-8166-5845)

16. Paul Guichard

University of Geneva, Department of Molecular and Cellular Biology, Sciences III,
Geneva, Switzerland
ORCID iD: [0000-0002-0363-1049](https://orcid.org/0000-0002-0363-1049)

17. Charles Coutton

Institute for Advanced Biosciences, (IAB), INSERM 1209, Institute for Advanced
Biosciences, (IAB) CNRS UMR 5309, Institute for Advanced Biosciences, (IAB)
Université Grenoble Alpes, UM de Génétique Chromosomique, Hôpital Couple-Enfant,
CHU Grenoble Alpes, F-38000 Grenoble, France

18. Selima Fourati Ben Mustapha

Polyclinique les Jasmins, Centre d'Aide Médicale à la Procréation, Centre Urbain
Nord, 1003 Tunis, Tunisia

19. Mahmoud Kharouf

Polyclinique les Jasmins, Centre d'Aide Médicale à la Procréation, Centre Urbain
Nord, 1003 Tunis, Tunisia

20. Raoudha Zouari

Polyclinique les Jasmins, Centre d'Aide Médicale à la Procréation, Centre Urbain
Nord, 1003 Tunis, Tunisia

21. Nicolas Thierry-Mieg

Laboratoire TIMC/MAGe, CNRS UMR 5525, Pavillon Taillefer, Faculté de Medecine,
38700 La Tronche, France

22. Serge Nef

Department of Genetic Medicine and Development, University of Geneva Medical
School, Geneva 1211, Switzerland
ORCID iD: [0000-0001-5462-0676](https://orcid.org/0000-0001-5462-0676)

23. Stefan Geimer

Cell Biology/ Electron Microscopy, University of Bayreuth, 95440 Bayreuth, Germany

24. Corinne Loeuillet

Institute for Advanced Biosciences, (IAB), INSERM 1209, Institute for Advanced Biosciences, (IAB) CNRS UMR 5309, Institute for Advanced Biosciences, (IAB) Université Grenoble Alpes

25. Pierre Ray

Institute for Advanced Biosciences, (IAB), INSERM 1209, Institute for Advanced Biosciences, (IAB) CNRS UMR 5309, Institute for Advanced Biosciences, (IAB) Université Grenoble Alpes, UM GI-DPI, CHU Grenoble Alpes, F-38000 Grenoble, France
ORCID iD: [0000-0003-1544-7449](https://orcid.org/0000-0003-1544-7449)

26. Christophe Arnoult

Institute for Advanced Biosciences, (IAB), INSERM 1209, Institute for Advanced Biosciences, (IAB) CNRS UMR 5309, Institute for Advanced Biosciences, (IAB) Université Grenoble Alpes

For correspondence:

christophe.arnoult@univ-grenoble-alpes.fr
ORCID iD: [0000-0002-3753-5901](https://orcid.org/0000-0002-3753-5901)

Editors

Reviewing Editor

Jean-Ju Chung

Yale University, United States of America

Senior Editor

Diane Harper

University of Michigan, United States of America

Reviewer #1 (Public Review):

In this study, Muroňová et al., demonstrate the physiological importance of a centriole and microtubule-associated protein, CCDC146, in sperm flagellar formation and male reproduction. In a previous study, the authors identified two loss-of-function mutations in CCDC146 from the sterile males with multiple morphological abnormalities in flagellar (MMAF) phenotype. To further test physiological significance of the CCDC146, the authors generate its knockout mouse model. The knockout males share the MMAF phenotypes with severely impaired flagellar morphology due to the defective sperm generation in testes. Using CCDC146 knock-in mouse model and expansion microscopy techniques, the authors observed CCDC146 localizes at human and mouse sperm flagella, which is different from the somatic cells. The authors also observed impaired manchette and head-tail coupling apparatus in developing spermatid lacking CCDC146 and address CCDC146 loss-of-function induces molecular and structural defects at axoneme in developing male germ cells, which finally causes MMAF phenotype and male infertility.

This reviewer agrees that identifying and analyzing new pathogenic molecules and variants is hugely valuable to establish male infertility in genetic level. As the authors have done, this

study also enlarges the genetic causality underlying MMAF and male infertility. In addition, this study applies new techniques, expansion microscopy, which is also an innovative approach. Although many approaches are used, unfortunately, this study misses the molecular mechanisms to explain pathogenicity to cause MMAF by the CCDC146. Only intracellular localization of the molecule is heavily examined. Although the authors show defective intracellular localization of the centriole and manchette, how CCDC146 loss-of-function and the developmental defects are linked is not examined. These limits provide the impression that this study could be simply another identification of the MMAF-causing gene, which were heavily performed by the authors. Also, in many parts, the results do not clearly support the authors claim. Therefore, this reviewer thinks the current manuscript requires additional results to clearly explain molecular mechanisms underlying the pathogenicity by CCDC146 loss-of-function.

Reviewer #2 (Public Review):

In whole exome sequencing of two patients suffering from MMAF syndrome, mutations of CCDC146 gene that result in premature stop codons were identified. The position of mutations could result in a truncated form of protein, thus whether these patients do indeed lack CCDC146 protein or if present, whether the truncated protein is functional, is unanswered by showing the CCDC146 protein localization only in the sperm from healthy donors. The main claim that CCDC146 protein is microtubule associated protein in the axoneme is well supported imaging expanded sperm flagellum to increase spatial resolution. However, the author's claim that the signal in the mid-piece is not specific is less supported by experimental evidence. The detection of CCDC146 in the sperm head is not further explored while TEM images show spermatogenesis defects in the manchette and acrosome formation. Increased detection of the CCDC146 protein in mouse sperm with sarkosyl supports its association with microtubules but does not exclude its potential role in the formation of sperm head. Overall, this study provides valuable information on CCDC146 function in male germ cells during spermatogenesis.

Reviewer #3 (Public Review):

Male infertility is an important health problem. Among pathologies with multiple morphological abnormalities of the flagellum (MMAF), only 50% of the patients have no identified genetic causes. It is thus primordial to find novel genes that cause the MMAF syndrome. In the current work, the authors follow up the identification of two patients with MMAF carrying a mutation in the CCDC146 gene. To understand how mutations in CCDC146 lead to male infertility, the authors generated two mouse models: a CCDC146-knockout mouse, and a knockin mouse in which the CCDC146 locus is tagged with an HA tag. Male CCDC146-knockout mice are infertile, which proves the causative role of this gene in the observed MMAF cases. Strikingly, animals develop no other obvious pathologies, thus underpinning the specific role of CCDC146 in male fertility.

The authors have carefully characterised the subcellular roles of CCDC146 by using a combination of expansion and electron microscopy. They demonstrate that all microtubule-based organelles, such as the sperm manchette, the centrioles, as well as the sperm axonemes are defective when CCDC146 is absent. Their data show that CCDC146 is a microtubule-associated protein, and indicate, but do not prove beyond any doubt, that it could be a microtubule-inner protein (MIP).

This is a solid work that defines CCDC146 as a novel cause of male infertility. The authors have performed comprehensive phenotypic analysis to define the defects in CCDC146 knockout mice. Surprisingly, the authors provide virtually no information on the penetrance

of those defects - in most cases they simply show descriptive micrographs. The message of this manuscript would have been more convincing if the key phenotypes of the CCDC146 knockout mice were quantified, in particular those shown in Fig. 2E, 7A, 11B, 13.

The manuscript text is well written and easy to follow also for non-specialists. The introduction and discussion chapters contain important background information that allow putting the current work into the greater context of fertility research. The figures could have been designed more carefully, with additional information on the genotype and other details such as the antibodies used etc. directly added to the figure panels, which would improve their readability. The author might also consider pooling small figures with complementary content into one bigger figure in order to group related information together, and again facilitate the reading of the manuscript.

Overall, this manuscript provides convincing evidence for CCDC146 being essential for male fertility, and illustrates this with a large panel of phenotypic observations, which however mostly lack quantification in order to judge their penetrance. Together, the work provides important first insights into the role of a so-far unexplored proteins, CCDC146, in spermatogenesis, thereby broadening the spectrum of genes involved in male infertility.